*J. Fluid Mech.* (2006), *vol.* 560, *pp.* 249–278.  
doi:10.1017/S0022112006000498 Printed in the United Kingdom

# Self-sustained acoustic-wave interactions with counterflow flames

By A. C. ZAMBON AND H. K. CHELLIAH

Mechanical and Aerospace Engineering, University of Virginia, Charlottesville, VA 22904, USA

(Received 28 March 2005 and in revised form 21 December 2005)

The interaction of acoustic waves with a planar counterflow flame is investigated numerically employing a detailed kinetic model and one-step global kinetic models. The mathematical formulation of quasi-one-dimensional fully unsteady laminar counterflow flames is presented and the governing equations are integrated numerically based on a MacCormack predictor–corrector scheme with second-order accuracy in space. Navier–Stokes characteristic boundary conditions are implemented to accurately represent perfect and partial reflection of acoustic waves at the boundaries. For well-resolved simulations, the occurrence of self-excited flame–acoustics instabilities is analysed in both non-premixed and premixed flames for a range of flow strain rates and flame locations, and employing two finite-rate kinetic models. Unlike the detailed kinetic model, one-step global models with large activation energy and overall reaction order greater than unity promote the amplification of acoustic pressure fluctuations in counterflow non-premixed flames. In contrast, premixed counterflow flames exhibit flame–acoustics instabilities with both kinetic models. While previous unsteady counterflow studies required external perturbations, the resonant unsteady phenomena predicted in this study are self-sustained under favourable boundary conditions. Detailed analyses of the characteristic time scales associated with convection, diffusion, chemistry and acoustics are presented to provide a better understanding of the exact coupling mechanisms.

## 1. Introduction

Understanding flame–acoustics coupling mechanisms that promote growth of combustion instabilities is of immense importance in many combustion systems. Linearized theories have provided considerable insight into the onset of the instabilities; however, application to complex flow geometries or highly nonlinear conditions is not straightforward. Furthermore, recent efforts to suppress combustion instabilities relying on model-based active-control approaches require accurate information about the nonlinear forcing terms driving the instability (Candel, Huynh & Poinsot 1996). The acoustic boundary conditions of the combustion device also play a significant role in determining the growth rate of the instability. Considering the complexity of the phenomenon, to address several fundamental issues in a systematic manner, the interaction of acoustic waves with a laminar *counterflow flame* is considered here. As described in this paper, not only are the characteristic transport and chemical time scales of importance, but the exact flame location with respect to pressure nodes and reactant flux nodes plays a significant role.

In an early theoretical investigation on the interaction of a planar flame with acoustic waves, by treating the flame as a gasdynamic discontinuity, Chu (1953)

developed an expression for the transfer function relating pressure change to the changes in flame speed, heat release, entropy, and ratio of specific heats. Under chemical non-equilibrium conditions, Toong *et al.* (1975) and Garris, Toong & Patureau (1975) (see Oran & Gardner 1985, for an extensive review) examined the chemical kinetic–acoustic coupling using an irreversible, one-step global kinetic model. While the global kinetic model employed by Toong *et al.* (1975) was general enough to include activation energy ($E_a$) as well as the overall reaction order ($m$) (i.e. molar reaction rate $\omega \sim Y^m \exp(-E_a/R^oT)$), the mathematical formulation neglected the transport effects across the flame structure. Consequently, their results are truly applicable to broad flames where convective terms, for example in the species conservation equations, are of the same order as the chemical kinetic rates. The maximum chemical kinetic–acoustic coupling was shown to occur when the ratio of characteristic chemical to acoustic time scales ($\tau_{chem}/\tau_{acou}$) approaches about 70. Exploiting the large activation energy and small Mach number ($M$) of the problem, van Harten, Kapila & Matkowsky (1984) extended the early work of Chu (1953) and Toong *et al.* (1975) to include more realistic flame structure and unsteady effects. Their formulation, however, was applied only to small-amplitude acoustic waves and flames having small heat release. In a subsequent investigation by Clavin, Pelcé & He (1990), finite heat release or gas expansion effects were analysed. Extensive complementary studies were also performed by McIntosh (1991, 1999) where the influence of characteristic length scales and time scales on the response of flames to acoustic perturbations was analysed. It was demonstrated that when the ratio of characteristic transport (or convective–diffusive) time scale to the acoustic time scale ($\tau_{transp}/\tau_{acou}$) approaches about 100, the chemical kinetics and acoustics couple leading to a significant growth of the unsteady pressure. In subsonic reacting flows with Mach number of the order of 0.002, $\tau_{transp}/\tau_{acou} = 100$ implies that the ratio of characteristic length of the pressure disturbance to the transport length scale ($N = \tau_{acou}/(M\tau_{transp})$), as defined in McIntosh (1991), is about 5, which is very similar to the counterflow configuration considered here.

The major weakness or uncertainty of all the previous theoretical investigations can be attributed to the simple global kinetic models employed, which is addressed in this paper via numerical integration of conservation equations employing both detailed and one-step global chemical kinetic models. As shown here, the chemical kinetic models have an enormous impact on the predicted unsteady pressure growth of the counterflow flames considered. In particular, based on a detailed analysis of the contributions of the reactions to the heat release, it is hypothesized here that the amplification of acoustic pressure fluctuations is promoted by strongly exothermic reaction steps with large values of activation energy.

In the present numerical investigation, the counterflow flame configuration with a planar flame established in the mixing layer created by two opposed streams is used. Such flames were first considered by Potter & Butler (1959) and Pandya & Weinberg (1963) (see Tsuji 1982, for a review of non-premixed counterflow flames). Here, both non-premixed and premixed flames are considered, as illustrated in figure 1. The fundamental standing acoustic waves established in this flow field under ideal boundary conditions, i.e. pressure nodes at the nozzle exits, are also shown in figure 1. Previous experiments on this configuration have failed to identify any self-sustained flame–acoustics interactions leading to such standing wave modes, primarily because of unfavourable boundary conditions at the nozzle exits, as discussed in this paper. The only exception is the recent investigation by Durox, Schuller & Candel (2002) where they have shown that a premixed flame established between a nozzle and

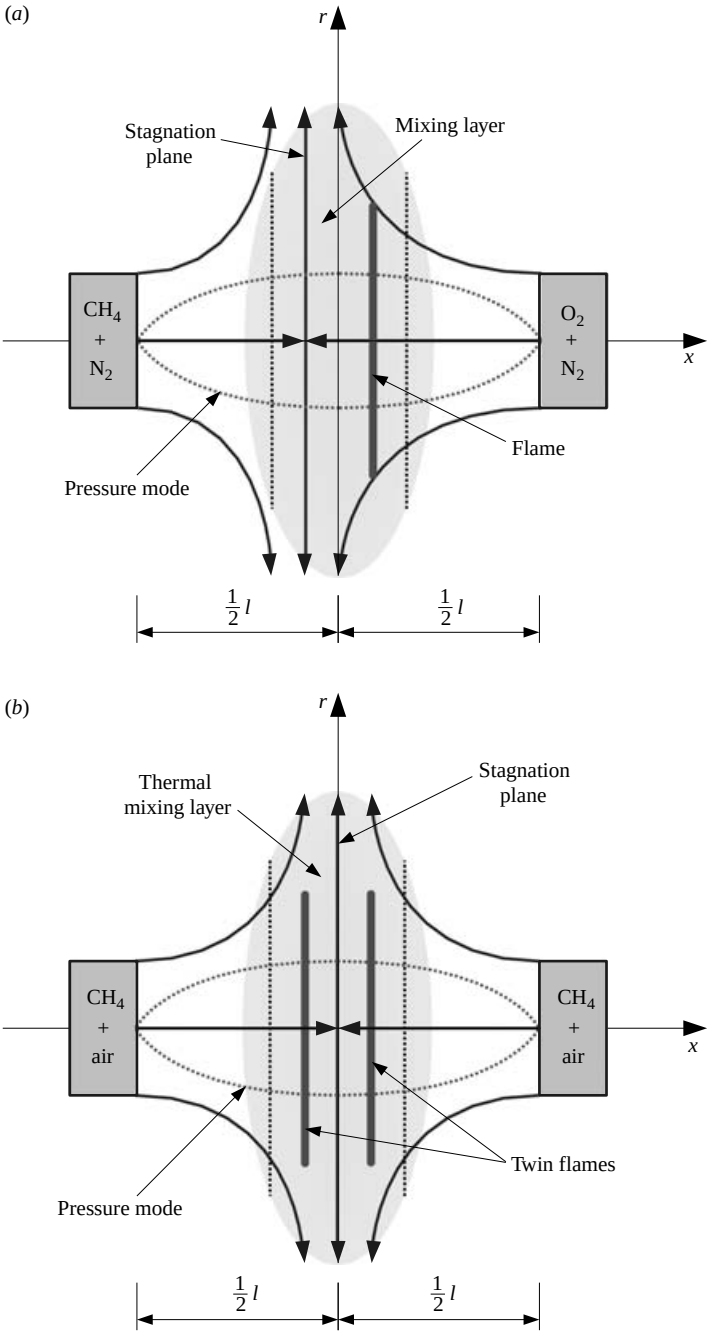


FIGURE 1. Illustration of the counterflow (*a*) non-premixed and (*b*) twin premixed flames with the dominant acoustic pressure mode.

a flat plate promotes self-excited acoustic waves; however the resonant frequency is determined by the length of the feed tube. Other unsteady counterflow flames investigated in the last decade were externally perturbed (Brown, Pitz & Sung 1998). The corresponding theoretical and numerical analyses of unsteady counterflow flames

fall into two categories identified by the method of external perturbation, namely (i) the pressure field is steady and uniform in space, and external perturbations are introduced via velocity fluctuations (Rogg 1989; Darabiha 1992; Im *et al.* 1995; Egolfopoulos & Campbell 1996) or (ii) the pressure field is uniform in space and oscillatory in time via external perturbation (Kim & Williams 1994; Sohn 2002).

In this paper, we solve for the general acoustic pressure field determined by the counterflow geometry. Consequently, we do not have the freedom to arbitrarily assign an oscillatory pressure frequency, as done by Kim & Williams (1994) or (Sohn 2002). The general formulation of the reacting counterflow field is presented first, followed in § 3 by the numerical approach employed, including the boundary conditions adopted. The self-similar governing equations derived include the full compressible effects. The response of a non-reacting counterflow field to an initial top-hat perturbation in pressure is presented in § 4 to establish the importance of boundary conditions and the necessary condition for acoustic pressure growth, i.e. existence of a flame in the counterflow field. The main results on non-premixed and premixed counterflow flame interactions with standing acoustic waves established between the two nozzles are presented in §§ 5 and 6, including the effects of flame location on the axial velocity node. A detailed analysis of characteristic flame time scales and exothermicity/endothermicity of heat release controlling the flame–acoustics interactions is presented in § 7.

## 2. Mathematical formulation

The mathematical formulation of quasi-one-dimensional fully unsteady laminar counterflow flames at low Mach numbers is systematically derived from the multi-dimensional chemically reacting compressible Navier–Stokes equations (Williams 1985), by assuming axisymmetry of the flow field and self-similarity of the solution. Both in the non-premixed and premixed configuration, counterflow flames are generally observed to take the form of a flat flame disk (Tsuji 1982). Because of this characteristic planar structure, for modelling purposes, it is reasonable to approximate the flame as *quasi-one-dimensional* in the neighbourhood of the axis of symmetry, i.e. the $x$-axis. Specifically, any variable $\phi(x, r, t)$ can be expanded in terms of $r$ about $r = 0$ as

$$\phi(x, r, t) = \phi_0(x, t) + \phi_1(x, t)r + \phi_2(x, t)r^2 + \ldots, \tag{2.1}$$

with first-order term, $\phi_1(x, t)$, identically zero based on symmetry considerations along the $x$-axis, the only exception being $u_1(x, t)$, the radial velocity component. After dropping the index notation and defining $u_1(x, t) \equiv U(x, t)$, the expansions for the density, $\rho$, the mass fraction of the $k$th species, $Y_k$, the axial velocity component, $v$, the radial velocity component, $u$ and temperature, $T$, are truncated at the leading order as $\rho(x, r, t) \simeq \rho(x, t)$, $Y_k(x, r, t) \simeq Y_k(x, t)$, $v(x, r, t) \simeq v(x, t)$, $u(x, r, t) \simeq U(x, t)r$, $T(x, r, t) \simeq T(x, t)$. With respect to pressure, $p$, the second-order term, $p_2(x, t)$, cannot be neglected *a priori* (Seshadri & Williams 1978) and it appears in the radial momentum equation as the pressure gradient in the radial direction, $\partial p/\partial r$. It is anticipated that the pressure can be expanded as

$$p(x, r, t) \simeq p_0(x, t) + p_2(x, t)r^2, \tag{2.2}$$

and the implications of $p_2$ are discussed in § 2.1. After substituting the self-similar form of the solution into the system of axisymmetric conservation equations, the resulting set of quasi-one-dimensional governing equations near the axis of symmetry

is given by

$$\frac{\partial \rho}{\partial t} + \frac{\partial \rho v}{\partial x} + 2\rho U = 0, \tag{2.3}$$

$$\frac{\partial \rho Y_k}{\partial t} + \frac{\partial \rho v Y_k}{\partial x} + \frac{\partial \rho Y_k V_k}{\partial x} + 2\rho Y_k U = W_k \omega_k, \tag{2.4}$$

$$\frac{\partial \rho v}{\partial t} + \frac{\partial \rho v v}{\partial x} + \frac{\partial p_0}{\partial x} + 2\rho v U = \frac{\partial}{\partial x}\left[\frac{4}{3}\mu\left(\frac{\partial v}{\partial x} - U\right)\right] + 2\mu\frac{\partial U}{\partial x}, \tag{2.5}$$

$$\frac{\partial \rho U}{\partial t} + \frac{\partial \rho v U}{\partial x} + 3\rho U^2 = -2p_2 + \frac{\partial}{\partial x}\left[\mu\frac{\partial U}{\partial x}\right], \tag{2.6}$$

$$\frac{\partial \rho h_t}{\partial t} - \frac{\partial p_0}{\partial t} + \frac{\partial \rho v h_t}{\partial x} + 2\rho h_t U = \frac{\partial}{\partial x}\left[\lambda\frac{\partial T}{\partial x}\right] - \sum_k \frac{\partial \rho Y_k V_k h_k}{\partial x} + \frac{\partial}{\partial x}\left[\frac{4}{3}\mu\left(\frac{\partial v}{\partial x} - U\right)v\right] + 2\mu\frac{\partial U}{\partial x}v - \frac{4}{3}\mu\left(\frac{\partial v}{\partial x} - U\right)U. \tag{2.7}$$

In these equations, $\mu$ designates the gas mixture viscosity, $\lambda$ the coefficient of thermal conductivity, and $h_t$ the total enthalpy, given by $h_t(x,t) = h(x,t) + (1/2)[v(x,t)]^2$. For the $k$th species, $Y_k$, $h_k$, $V_k$, $W_k$ and $\dot{\omega}_k$ represent the mass fraction, enthalpy, diffusion velocity, molecular weight and molar chemical production rate, respectively. Near the axis of symmetry, the thermodynamic effects of the radial pressure gradient due to $p_2$ are negligible. Thus, the leading-order term for pressure $p_0$ is related to the other thermodynamic variables by the equation of state for a mixture of perfect gases, given by $p_0 = \rho RT$, where $R = R^o/\overline{W}$ with $R^o$ being the universal gas constant and $\overline{W}$ the mean molecular weight of the mixture.

### 2.1. *Representation of the pressure field*

In the well-known steady-state formulation of Seshadri & Williams (1978), the isobaric assumption along the $x$-axis, i.e. $p_0 = \text{const}$, is usually introduced for low-Mach-number flows, resulting in an axially uniform as well as steady pressure field given by $p(x,r,t) = p_0 + \frac{1}{2}\mathscr{J}r^2$, where both $p_0$ and $\mathscr{J} = 2p_2$ are constants, the latter being the eigenvalue of a two-point boundary value problem, $\mathscr{J} = (1/r)(\partial p/\partial r)$. The eigenvalue, which is related to the flow strain rate in the counterflow field, is a function of the nozzle separation distance, $l$, and of the flow velocity imposed at the boundaries, i.e. $v_{\pm l/2}$. For a steady, non-premixed flame, the characteristic flow strain rate is typically defined as the axial velocity gradient $a = \mathrm{d}v/\mathrm{d}x$ at the edge of the mixing layer on the oxidizer side (Chelliah *et al.* 1990). A similar definition is extended to counterflow premixed flames by considering the edge of the thermal mixing layer on the side of the combustible mixture. In the present unsteady formulation, the leading-order pressure term, $p_0(x,t)$, appears in the conservation equations for axial momentum (2.5) and energy (2.7), and the second-order pressure term, $p_2$, appears in equation (2.6) which accounts for the radial flow via the pressure gradient in the radial direction. Unlike other dependent variables, the description of these pressure terms requires careful attention in the derivation of a self-similar, fully unsteady, compressible formulation. Expressing $p_0(x,t)$ as the sum of the mean uniform pressure and of the acoustic pressure fluctuation, i.e. $p_0 = \bar{p}_0 + p_0'(x,t)$, (2.2) can be written as $p(x,r,t) = \bar{p}_0 + p_0'(x,t) + p_2(t)r^2$. Such a decomposition of pressure facilitates the investigation of flame–acoustics interaction about the mean or steady-state pressure of $\bar{p}_0$, while the unsteady pressure is accounted for by the terms $p_0'(x,t)$ and $p_2(t)$.

In the analysis of Rogg (1989) and others, the unsteady pressure effects were allowed via $p_2(t)$ only, with the implicit assumption that $p_0'(x,t) \equiv 0$. The temporal variation of the radial pressure eigenvalue resulted in the strain rate variation in time, with the axial pressure remaining constant in space and time. In contrast, Kim & Williams (1994) and Sohn (2002) have assumed that the unsteady pressure effects can be modelled with $p_0'$ function of time only and $p_2(t) =$ constant. The latter assumption implies that the eigenvalue remaines constant during the flame–acoustics interaction. One common feature of all previous investigations was the neglect of the spatial dependence of the unsteady pressure, i.e. $\partial p_0/\partial x$ in (2.5), the fundamental reason for requiring an external perturbation. In this work, self-sustained geometry-dependent resonant acoustic waves arise by retaining the full spatial and temporal variation of acoustic pressure via the term $p_0'(x,t)$. The only limitation imposed is the constant $p_2(t)$ term implying that during the growth of the unsteady pressure, the pressure eigenvalue remains constant, or in other words the mean flow strain rate remains constant. It should be pointed out that the instantaneous strain rate still varies because of the spatial variation of $p_0'(x,t)$, as discussed below.

### 2.2. *Axial momentum equation at low Mach number*

In previous counterflow formulations, the axial momentum equation, both in the steady (Smooke *et al.* 1990) and unsteady formulation (Rogg 1989; Im *et al.* 1995), was inconsequential under the assumption of a spatially uniform pressure field. However, the present flame–acoustics investigation with standing acoustic waves, requires integration of the axial momentum conservation equation (2.5) (or a simplified version at the low-Mach-number limit), yielding the acoustic pressure component, $p_0'(x,t)$. Let $(\,)^*$ denote a non-dimensional variable and $(\,)_R$ a reference-state variable, with dimensional variables expressed as $\rho = \rho^* \rho_R$, $v = v^* v_R$, $p = p^* p_R$, $t = t^* t_R$, $x = x^* l$. For a mixture of ideal gases, the speed of sound is $c = \sqrt{\gamma RT} = \sqrt{\gamma p/\rho}$. Consequently, the appropriate reference pressure is then defined as $p_R = c_R^2 \rho_R/\gamma_R$. The relevant reference time scale is the acoustic time scale, which can be defined as $t_R = l/c_R$, where $l$ is the separation distance of the nozzles. With the above definitions, the non-dimensional form of the momentum equation, neglecting viscous losses, can be then written as

$$\left[\frac{1}{M}\right] \frac{\partial \rho^* v^*}{\partial t^*} + \frac{\partial \rho^* v^* v^*}{\partial x^*} + \left[\frac{1}{\gamma_R M^2}\right] \frac{\partial p^*}{\partial x^*} = 0, \tag{2.8}$$

where $M = v_R/c_R$ is the Mach number. For low-Mach-number flows, each non-dimensional variable can be expanded in terms of this small parameter, e.g. $\rho^* = \bar{\rho}^* + \rho'^* M + \cdots$, $p^* = \bar{p}^* + p'^* M + \cdots$. It follows that, to the leading order $O[1/M^2]$, the isobaric condition on $\bar{p}^*$ must be satisfied, which in terms of dimensional thermodynamic pressure yields

$$\frac{\partial \bar{p}_0}{\partial x} = 0. \tag{2.9}$$

The above equation has been used in all previous steady-state and unsteady counterflow formulations. At the next higher order, $O[1/M]$, the effect of $p'^*$ becomes relevant and the following equation for the dimensional acoustic pressure $p_0'(x,t)$ is obtained:

$$\frac{\partial \rho v}{\partial t} + \frac{\partial p_0'}{\partial x} = 0. \tag{2.10}$$

In the current formulation, $\bar{p}_0$ is assumed uniform from equation (2.9) and the effects of $p_0'(x,t)$ are evaluated using equation (2.10).

## 3. Numerical method

The numerical integration of the governing equations is performed using an explicit MacCormack predictor–corrector scheme, widely used in the literature for compressible flows (Fletcher 1988). Recasting the system of partial differential equations in conservative form and adopting a compact vectorial notation, the relevant terms in the numerical scheme can be identified,

$$\frac{\partial \boldsymbol{Q}}{\partial t} + \frac{\partial \boldsymbol{F}}{\partial x} = \frac{\partial \boldsymbol{R}}{\partial x} + \boldsymbol{S}, \tag{3.1}$$

where $\boldsymbol{Q}$ is the vector of conserved variables, $\boldsymbol{F}$ the convective flux vector, $\boldsymbol{R}$ the diffusive flux vector and $\boldsymbol{S}$ the source terms vector. In the predictor–corrector approach, the vector of conserved variables, $\boldsymbol{Q}$, is updated by downwind differencing the convective flux vector, $\boldsymbol{F}$, in the predictor step, and by upwind differencing in the subsequent corrector step. At all iterations, the derivative of $\boldsymbol{R}$, the diffusive flux vector, is always discretized in the direction opposite to that of the derivative of $\boldsymbol{F}$. In order to eliminate any directional bias, at each iteration the differencing direction of all spatial derivatives is reversed (Zambon 2005). Despite the availability of higher-order numerical schemes, the present approach is more than adequate to gain a fundamental understanding of the physical and chemical coupling mechanisms driving flame–acoustics instabilities.

### 3.1. *Boundary and initial conditions*

For the two opposed nozzles, the pressure nodes are assumed to be located close to the exits of the nozzles (open-tube boundary conditions). With fixed temperature and species mass fractions of inflow streams, the following physical boundary conditions are imposed: at $x = x_{-\infty} = -l/2$,

$$p = p_{-\infty}, \quad Y_k = Y_{k,-\infty}, \quad U = 0, \quad T = T_{-\infty}; \tag{3.2}$$

and at $x = x_{\infty} = +l/2$,

$$p = p_{\infty}, \quad Y_k = Y_{k,\infty}, \quad U = 0, \quad T = T_{\infty}. \tag{3.3}$$

The axial velocities at the boundaries are prescribed through the implementation of Navier–Stokes characteristic boundary conditions (NSCBC) (see Poinsot & Lele 1992), the choice of which can yield perfect and partial reflection of acoustic waves at the boundaries. In the NSCBC approach, there are generally two characteristic waves travelling into the domain through the inflow boundary (their amplitudes being $L_2$ and $L_5$), and one characteristic wave travelling from the interior of the domain to the inlet with amplitude $L_1$. For perfect reflection of acoustic waves,

$$L_1 = (v - c)\left[\frac{\partial p_0}{\partial x} - \rho c \frac{\partial v}{\partial x}\right], \tag{3.4}$$

$$L_2 = 0, \tag{3.5}$$

$$L_5 = -L_1, \tag{3.6}$$

and the axial velocity is updated at the inlets by integrating,

$$\frac{\partial \rho v}{\partial t} + v\frac{1}{c^2}\left[L_2 + \frac{1}{2}(L_5 + L_1)\right] + \frac{1}{2c}\left[L_5 - L_1\right] = 0. \tag{3.7}$$

The assumption of pressure nodes located at the exits of the nozzles can be relaxed by allowing partial reflection of acoustic waves. In this case, the predicted amplitude

of incoming waves can be modified by varying the parameter $\sigma$ in

$$L_5 = \sigma(p_0 - \bar{p}_a), \tag{3.8}$$

where $\bar{p}_a$ is the atmospheric pressure in the far field, and by updating the density or equivalently the pressure at the inlets:

$$\frac{\partial \rho}{\partial t} + \frac{1}{c^2}\left[L_2 + \frac{1}{2}(L_5 + L_1)\right] = 0. \tag{3.9}$$

The initial conditions for the time-dependent governing equations are provided by the counterflow steady-state solution, evaluated at the same mean flow conditions. This initial solution is obtained numerically from a modified version of the steady-state code developed by Smooke *et al.* (1990). Since this initial solution relies on the isobaric assumption and is based on a slightly different discretization scheme, when employed as input in the unsteady code, it adjusts itself to the full compressible equations described in § 2, during a brief transient. This numerical adjustment results in the generation of acoustic waves over a broad frequency spectrum and automatically introduces some acoustic disturbance in the physical domain, typically of the order of 2–5 Pa. The sensitivity of the self-excited acoustic pressure growth rate to the initial acoustic perturbation was investigated by exciting the dominant frequency over several cycles as well as introducing a top-hat pressure profile yielding a broad-band perturbation up to about 10 Pa. Depending on the selection of boundary conditions, acoustic waves travel across the domain and are reflected at the boundaries. Based on the acoustics of the system, only its natural frequencies can potentially be excited, while the remaining noise is dissipated. It is anticipated that if an acoustic coupling with the flame is established, the resulting resonant interaction is self-sustained, without any external excitation.

### 3.2. *Grid resolution and time step size*

In the problem under investigation, an accurate resolution of the flame structure is critical, in particular in the reactive–diffusive region of the flame, where sharp gradients in the concentrations of the minor species are present together with a very sharp heat release rate profile. Therefore, high spatial resolution of the grid is required across the flame structure established between the two opposed nozzle exits. Depending on the flow strain rate, which generally controls the flame thickness, extensive grid resolution investigations have indicated that the required minimum $\Delta x$ in this region is estimated in the range 5–15 μm (Zambon 2005). For some cases, to reduce the computational effort, a stretched grid with a high resolution in the chemically reacting region and at the boundaries (because of pressure nodes at the boundaries) is considered, while in the rest of the spatial domain the grid is smoothly stretched using a stretching function proposed by Roberts (see Fletcher 1988). Because of the explicit nature of the selected MacCormack numerical scheme, the major limitation is imposed by the CFL condition on the numerical stability of the method. Since a high spatial resolution of the grid is employed, the largest time step size allowed is estimated to be around $10^{-8}$ s, based on the local speed of sound. Furthermore, the characteristic time scales of physical and chemical phenomena involved are estimated to range from $10^{-7}$ to $10^{-2}$ s. Considering the above time scales, the selected time step size is more than adequate to capture the dynamics of all the phenomena, including the resolution of the fastest chemical time scales. Calculations are usually carried out to cover 10 ms of physical time or about 200 acoustic-wave interactions with the flame based on $\tau_{acou} \simeq 5 \times 10^{-5}$ s (see § 7.2). Although relatively short, this time interval is

adequate to investigate the initial triggering of flame–acoustics instabilities and the subsequent establishment of self-excited resonant acoustic modes characterizing the growth rate in the linear instability regime.

### 3.3. *Chemical kinetic models*

A detailed chemical kinetic model for methane–air combustion consisting of 17 species in 39 elementary reactions (Peters & Rogg 1993) is used in the present simulations of unsteady non-premixed and premixed counterflow flames. Previous studies have shown that this detailed model yields flame extinction predictions of non-premixed flames (Chelliah, Seshadri & Law 1993) and burning velocity of premixed flames (Mauss & Peters 1993) in close agreement with experiments. For the purpose of analysis and comparison with previous theoretical work employing different values of activation energy and overall reaction orders, several one-step global models are derived as described in the Appendix. For example, the reaction rate of a stoichiometric one-step global model $CH_4 + 2O_2 \rightarrow CO_2 + 2H_2O$, is represented by

$$\omega_{1-step} = c_{CH_4}^{\alpha} c_{O_2}^{\beta} A \exp(-E_a/R^o T), \tag{3.10}$$

where $\alpha$ and $\beta$ are the reaction orders with respect to the reactants (with overall reaction order $m = \alpha + \beta$), and $A$ and $E_a$ are Arrhenius rate constants representing the collision frequency and the activation energy, respectively. For selected values of $\alpha$, $\beta$, and $E_a$, the collision frequency, $A$, is varied to give a similar flame extinction condition for a steady, non-premixed flame or the burning speed of a steady premixed flame, as described in the Appendix.

## 4. Acoustic response of chemically non-reacting counterflow

In order to assess the accuracy of the numerical method and of the implementation of boundary conditions, calculations are first performed in the chemically non-reacting counterflow field. Figure 2(*a*) shows the steady-state species profiles along the axis of symmetry at a flow strain $a = 412\,\mathrm{s}^{-1}$, with methane being delivered from the left boundary ($x = -l/2 \equiv -0.5\,\mathrm{cm}$) and air from the right boundary ($x = +l/2 \equiv 0.5\,\mathrm{cm}$). At $t = 0\,\mathrm{s}$, a top-hat perturbation in pressure with $-50\,\mathrm{Pa}$ is introduced as shown in figure 3(*a*) and the resulting emergence of a broad-band of acoustic waves travelling back and forth in the spatial domain is tracked for 10 ms. For the most favourable case involving perfectly reflecting boundary conditions, figure 3(*b*) shows diminished standing acoustic pressure waves, $p_0'(x, t)$, saved (every 1000 time steps) over a period of the fundamental mode of around $t = 10\,\mathrm{ms}$, with no clear resonating acoustic mode. If the numerical integrations are carried out further, completely random acoustic waves travelling across the spatial domain are observed. The rate of decay of the acoustic waves generated by the initial perturbation can be accelerated by imposing partially reflecting boundary conditions by varying the value of $\sigma$ in (3.8), as shown in figure 4. Here, $\sigma$ has units of $\mathrm{s}^{-1}$, whence the value $\sigma = 10^8$ corresponds to $O(10^3)$ after normalization with respect to the characteristic acoustic time, $\tau_{acou}$ (note that normalized time $\equiv t/\tau_{acou}$ in all plots depicting the acoustic pressure variation with time). Any decrease of $\sigma$ essentially moves the pressure nodes away from the nozzles exit locations, hence damping the reflected pressure waves. In order to investigate flame–acoustics coupling at different flow strain rates (corresponding to varying inflow velocities), the influence of the strain rate on the decay of the initially perturbed pressure field in the non-reacting flow field is also investigated. Figure 5 compares the acoustic pressure fluctuations, $p_0'(x, t)$, at the mid-point of the

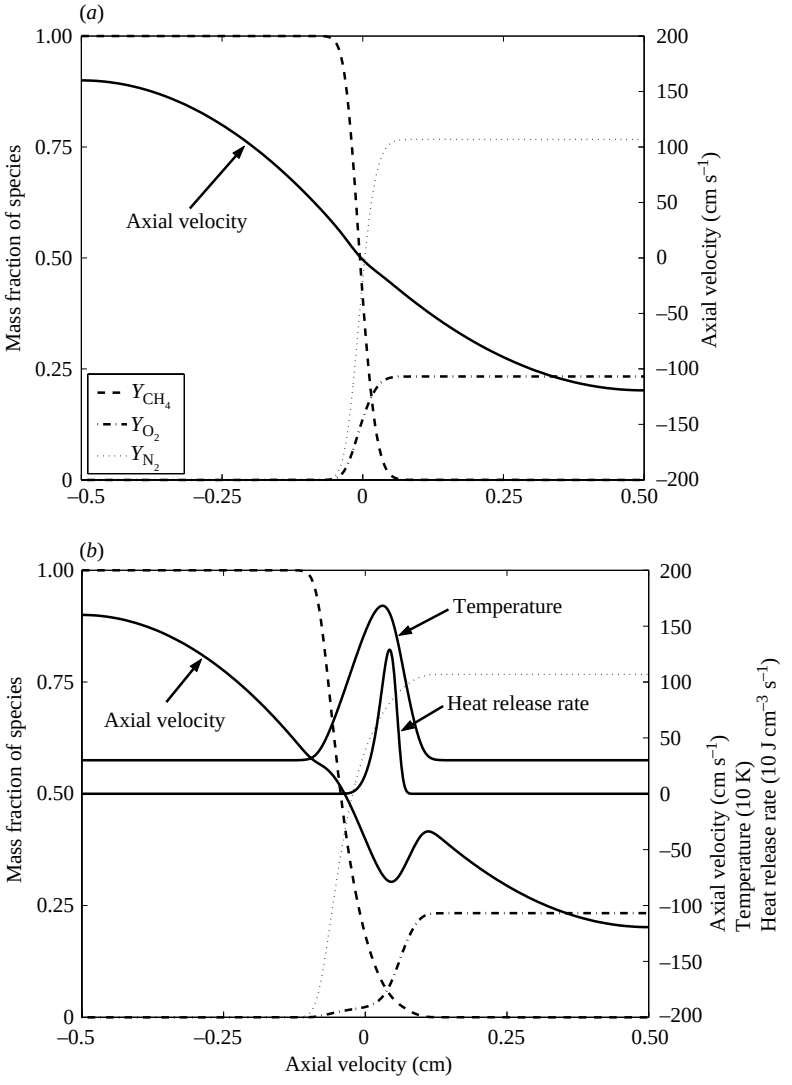


FIGURE 2. Representation of the mixing layer of the counterflow methane–air non-premixed configuration without and with flame ignited. (*a*) Chemically non-reacting conterflow field at $a = 412\,\mathrm{s}^{-1}$. (*b*) Counterflow non-premixed flame at $a = 416\,\mathrm{s}^{-1}$.

domain for a low ($a = 118\,\mathrm{s}^{-1}$) and high ($a = 412\,\mathrm{s}^{-1}$) flow strain rates. As perfectly reflecting boundary conditions are used, the rate of decay is rather slow, since no losses of acoustic energy are allowed at the boundaries. The only mechanism for dissipation is due to viscous effects. The rate of decay is larger at the higher strain rate since the components of the gradient of velocity are much larger and so is the viscous dissipation. The above non-reacting numerical integrations indicate that irrespective of the acoustic pressure boundary conditions imposed or of the strain rate, the acoustic pressure decays in the absence of a flame.

## 5. Counterflow non-premixed flames

When ignited, the typical structure of a steady counterflow non-premixed methane–air flame at a flow strain rate $a = 416\,\mathrm{s}^{-1}$ is shown in figure 2(*b*), where the species

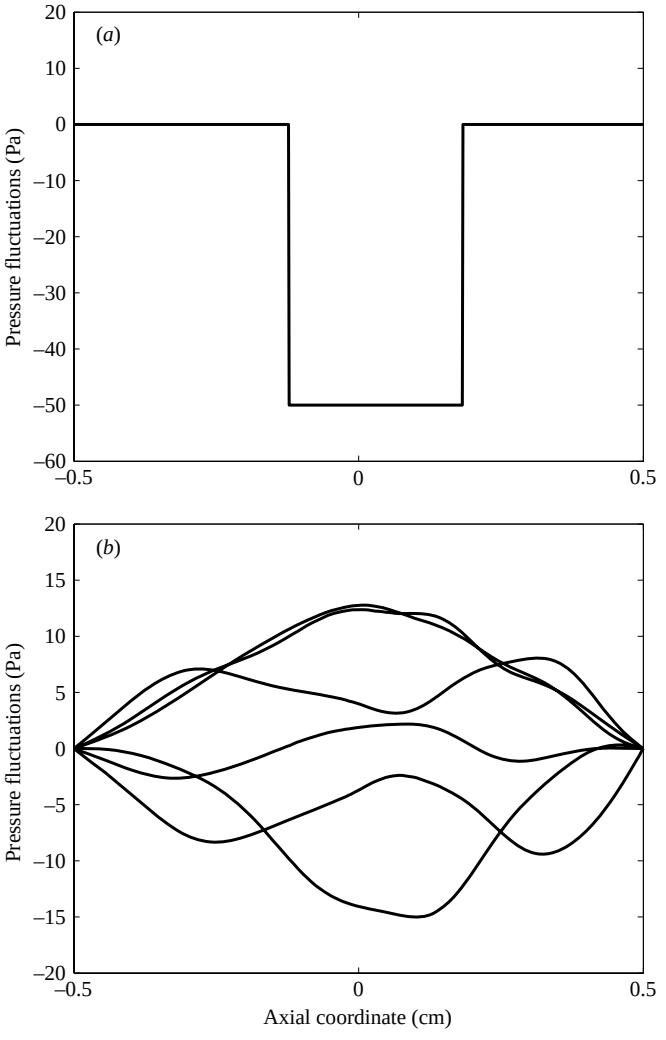


FIGURE 3. Representation of (*a*) the initial top-hat pressure perturbation and (*b*) the acoustic pressure profiles saved (every 1000 time steps) over a period of the fundamental mode around $t = 10$ ms for a chemically non-reacting counterflow field.

and thermal mixing layers are highlighted. Similarly to the chemically non-reacting case considered previously, methane is delivered from the left and air from the right. The axial velocity and heat release profiles are also shown. The response of such steady counterflow flames to various pressures, velocities and compositions have been investigated extensively (Tsuji 1982). The steady-state solution is used as the starting point for the unsteady computations. In order to retain the acoustic energy in the physical domain and create the conditions most favourable for the onset of flame–acoustics instabilities, perfectly reflecting boundary conditions (3.4)–(3.6) are implemented. Due to subtle differences between the numerical schemes for steady and unsteady computations, the initial steady-state flame solution automatically introduces an initial acoustic disturbance so that no additional initial perturbation is required. Because of the flexibility provided by the present computational approach in adopting a wide range of chemical reaction models, the influence of chemical kinetics on the

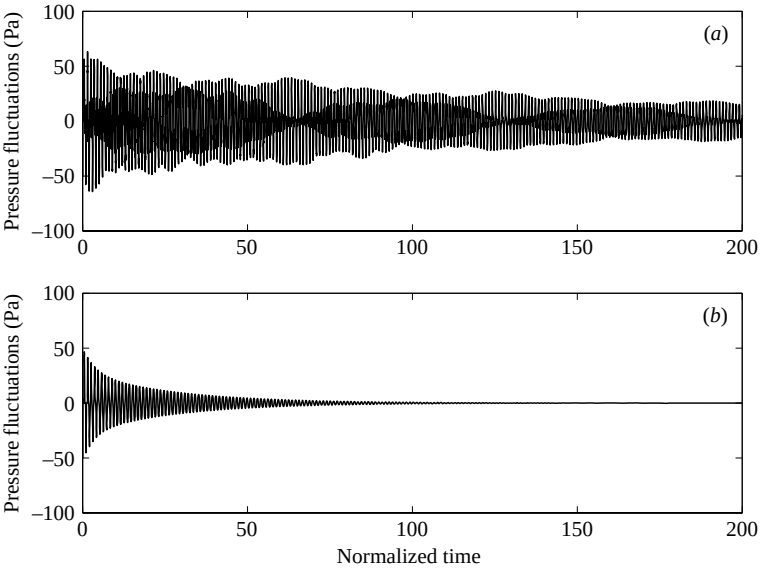


FIGURE 4. Effect of partial reflection of acoustic waves at the boundaries in terms of the parameter $\sigma$ on the decay of acoustic pressure fluctuations at $x = 0$ in the chemically non-reacting counterflow field. (*a*) $\sigma = 10^8\ \mathrm{s}^{-1}$, (*b*) $\sigma = 10^6\ \mathrm{s}^{-1}$.

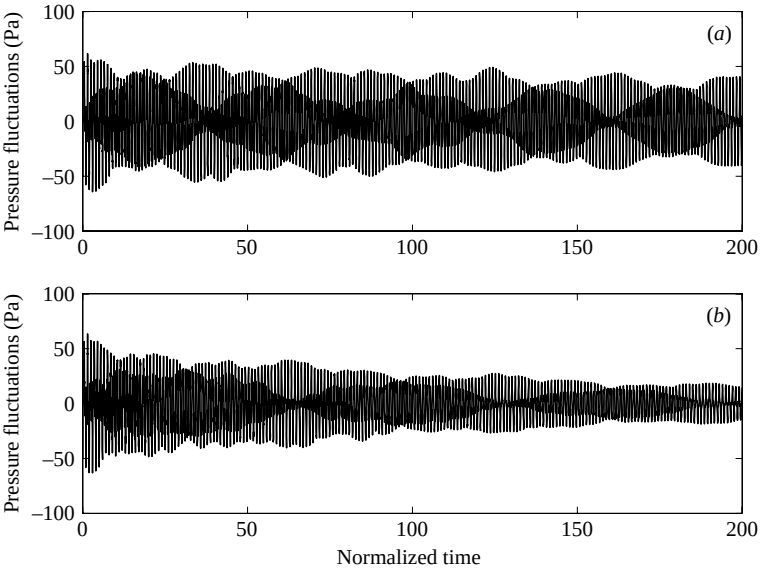


FIGURE 5. Effect of strain rate on the decay of acoustic pressure fluctuations in the chemically non-reacting counterflow field with perfectly reflecting boundary conditions. (*a*) $a = 118\ \mathrm{s}^{-1}$, (*b*) $a = 412\ \mathrm{s}^{-1}$.

flame–acoustics coupling mechanism can be addressed. Figure 6 shows the evolution in time of the predicted acoustic pressure fluctuations, $p_0'(x, t)$, evaluated at $x = 0$, for a low strain rate of $50\ \mathrm{s}^{-1}$ and a near-extinction strain rate of $416\ \mathrm{s}^{-1}$. Results are presented for two reaction models, the detailed model of Peters & Rogg (1993) and a one-step model with activation energy of $125.5\ \mathrm{kJ\,mol}^{-1}$ (or $30\ \mathrm{kcal\,mol}^{-1}$)

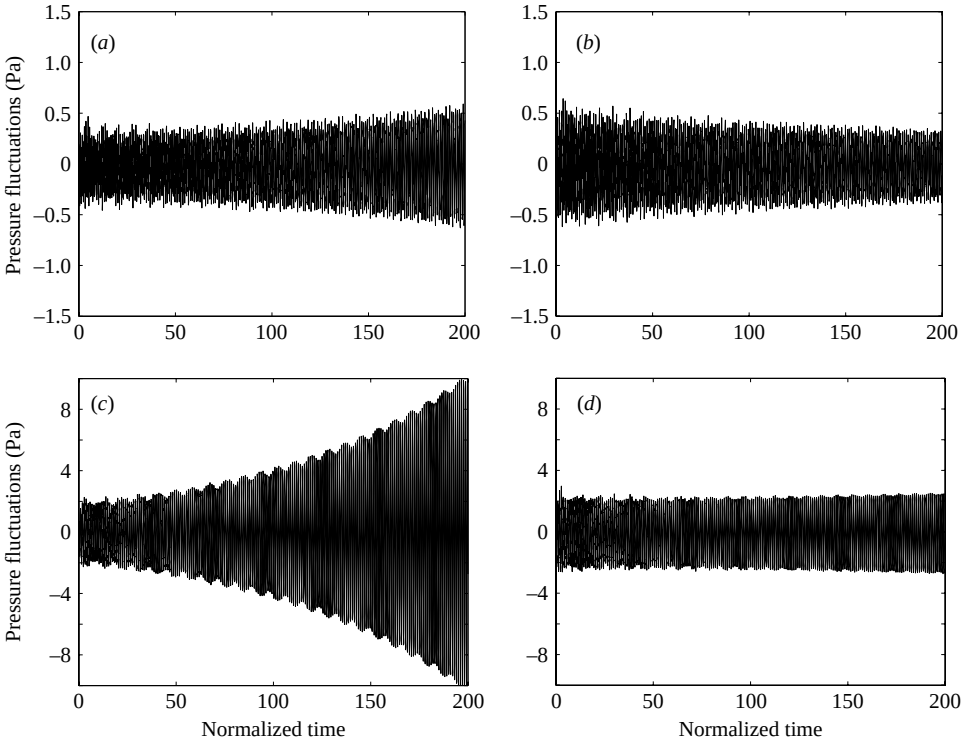


FIGURE 6. Effect of flow strain rate on the acoustic response of counterflow non-premixed flames using a one-step model (with $E_a = 125.5\,\mathrm{kJ\,mol^{-1}}$ and $\alpha = \beta = 1$) and the detailed kinetic model. (*a*) One step at $a = 50\,\mathrm{s^{-1}}$. (*b*) Detailed at $a = 50\,\mathrm{s^{-1}}$. (*c*) One-step at $a = 416\,\mathrm{s^{-1}}$. (*d*) Detailed at $a = 416\,\mathrm{s^{-1}}$.

and reaction orders $\alpha = \beta = 1$ (see the Appendix for details). The one-step kinetic model exhibits amplification of $p_0'$ regardless of the strain rate, whereas the detailed model shows decay at $a = 50\,\mathrm{s^{-1}}$ and almost no growth at $a = 416\,\mathrm{s^{-1}}$. The significant difference in acoustic response between the two kinetic models is a novel finding. Because of the prevalent use of such one-step models in analytical studies of flame–acoustics instabilities, with and without flow straining (McIntosh 1991; McIntosh, Brindley & Yang 2002), as well as in multi-dimensional flame stability investigations (Matalon & Matkowsky 1982; Keller & Peters 1994; Wu *et al.* 2003), these results suggest significant implications.

While the influence of flow strain rate, as seen in figure 6, can be related to the shift in transport time scales, the effect of chemical kinetics due to the specific kinetic model employed requires further analysis. For a high flow strain rate of $416\,\mathrm{s^{-1}}$ corresponding to near-extinction conditions, figure 7(*a*) compares the predicted acoustic pressure growth rates of one-step kinetic models with reaction orders of $\alpha = \beta = 1$ (overall reaction order $m = 2$) and with varying activation energy. A distinct increase in the pressure growth rate is seen for large activation energies, consistent with the analytical results employing one-step models reported by Garris *et al.* (1975) and McIntosh (1991). The activation energies selected here of 62.8, 125.5 and 188.3 kJ $\mathrm{mol^{-1}}$ (15, 30, and 45 in kcal $\mathrm{mol^{-1}}$) correspond to the non-dimensional activation energies of $\theta = 3.4, 6.8$ and 10.3 considered by McIntosh (1991), respectively. For comparison, the predicted acoustic pressure growth rate with the detailed reaction

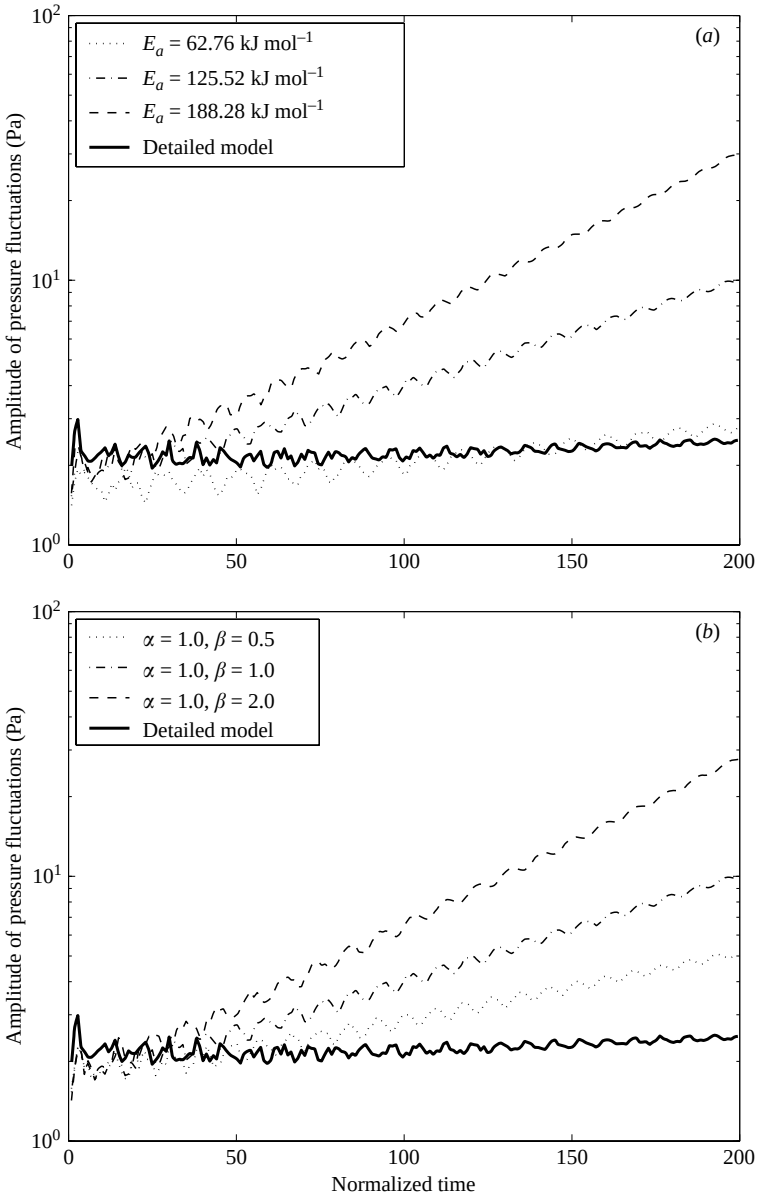


FIGURE 7. Comparison of the acoustic pressure growth rate of a counterflow non-premixed flame at $a = 416\,\mathrm{s}^{-1}$ between the detailed and one-step kinetic models with (*a*) varying $E_a$ and $\alpha = \beta = 1$, and (*b*) varying $\beta$ and $E_a = 125.5\,\mathrm{kJ\,mol}^{-1}$ and $\alpha = 1$.

model is also shown in figure 7(*a*), indicating close agreement with the result for the one-step model with lower activation energy.

Besides the nonlinearity associated with activation energy, the reaction orders with respect to the reactants can also directly influence the flame–acoustics coupling mechanism. For an activation energy of $125.5\,\mathrm{kJ\,mol}^{-1}$ in the one-step model, the variation of the reaction order with respect to $O_2$, that is $\beta$, on the predicted acoustic pressure growth is shown in figure 7(*b*). The selection of $\beta$ instead of $\alpha$, the reaction

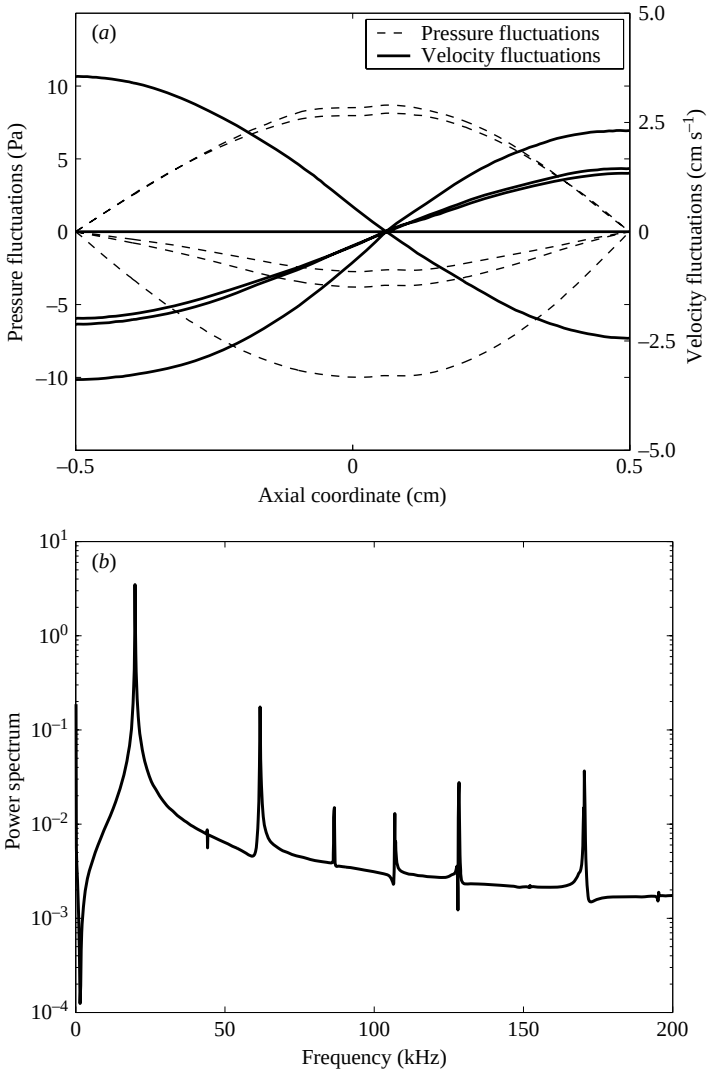


FIGURE 8. Representation of (*a*) the dominant acoustic pressure and velocity profiles saved (every 1000 time steps) over a period of the fundamental mode and (*b*) the frequency power spectrum of $p_0'$ at $t = 10$ ms for a resonant case with a one-step kinetic model with $E_a = 125.5$ kJ mol$^{-1}$ and $\alpha = \beta = 1$.

order with respect to $CH_4$, as the more relevant kinetic parameter is based on a sensitivity analysis conducted for $E_a = 125.5$ kJ mol$^{-1}$ around $\alpha = \beta = 1$. While the predicted trends are consistent with those of Garris *et al.* (1975) and Kim & Williams (1994), comparison with the detailed model indicates that the overall reaction order $m$ is perhaps less than 1.5 at the selected overall activation energy of 125.5 kJ mol$^{-1}$. Under favourable conditions, e.g. at high strain rate employing a one-step kinetic model with large activation energy, the non-premixed flame–acoustics interaction leads to the establishment of standing waves as shown in figure 8(*a*). The mode shapes shown are based on several solutions of $p_0'(x, t)$ saved over a period of the fundamental mode (i.e. at every 1000 time steps or every $10^{-5}$ s) of about $t =$ 10 ms. The dominant half-wave mode shape of the acoustic pressure is consistent

with the open-tube boundary condition of the opposed nozzles. Also shown are the corresponding acoustic fluctuations in axial velocity as well as the calculated power spectrum based on the unsteady pressure at $x = 0$ (figure 8*b*). The latter was evaluated using the results saved over the entire time history of 10 ms, whence relating the power spectra to sound level in dB can be misleading. On the other hand, if the unsteady pressure result at about 10 ms is used (at the mid-point of the domain), for $p_{rms} = 7$ Pa shown in figure 8(*b*), the sound level of 110 dB is obtained (note: the corresponding sound level using the detailed model predictions at about 10 ms is 98 dB).

The most important quantitative information realizable from figure 8(*b*) is the dominant half-wave mode frequency of 19.5 kHz, followed by the full-wave mode, three-half-wave mode, etc. This dominant frequency for the nozzle separation distance of 1 cm corresponds to an acoustic velocity of $\sim 400\,\mathrm{m\,s^{-1}}$ estimated at an average temperature of $\sim 400$ K across the physical domain. The observed lower power of the second mode, i.e. full-wave, compared to the three-half-wave mode is an artifact of the location of the pressure transient used in evaluating the Fourier transform, i.e. the mid-point of the computational domain which corresponds to a pressure node for the full-wave mode. The major distinction between the present and previous unsteady modelling efforts (Darabiha 1992; Im *et al.* 1995; Egolfopoulos & Campbell 1996; Sohn 2002) is that the acoustic phenomenon predicted here is self-sustained, i.e. no external velocity perturbations are imposed. The growth of the unsteady pressure is a direct consequence of the interaction between acoustic pressure and combustion kinetics.

### 5.1. *Effect of non-premixed flame location*

In counterflow flames, the flame location can be altered by two methods, namely (*a*) by unbalancing the axial momenta of the fuel and air streams and (*b*) by varying the mixture composition. The latter approach, however, can drastically change the flame structure and flame extinction conditions. For this reason, only the flame shift due to the unbalanced momenta is analysed here and the condition $(\rho v^2)_{-l/2} = (\rho v^2)_{+l/2}$ usually employed in experiments (Chelliah *et al.* 1990) is relaxed. As shown in figures 9(*a*) and 9(*b*), $CH_4$ is delivered to the flame front from the left and $O_2$ from the right. In the illustrations, the flame is identified by the spatial profile of the heat release rate. Naturally occurring acoustic fluctuations in axial velocity induce a modulation of the transport of the reactants to the flame. Since there are two separate fluxes, namely of methane and air, the modulation can occur in different degrees and with different phases with respect to each other. Specifically, depending on the relative position of the flame with respect to the velocity node, the phase difference between oscillations in pressure and in the mass flux of reactants can either be $90^\circ$ or $-90^\circ$ (Candel *et al.* 1996). Using the Rayleigh criterion (Rayleigh 1878), the corresponding fluctuation in heat release rate can then be in-phase or out-of-phase with the pressure fluctuations and therefore lead to amplification or decay of acoustic pressure fluctuations. In the counterflow configuration with $v > 0$ for the methane stream and $v < 0$ for the air stream (see figure 2*b*), when the fluxes at the inlet are slightly increased due to a velocity perturbation ($v'|_{x=-l/2} > 0$ and $v'|_{x=l/2} < 0$), $v'$ can contribute to either an increase or a decrease in the delivery of the reactants to the flame front depending on the specific flame location in the physical domain. In figures 9(*a*) and 9(*b*), fluxes of fuel and oxidizer are denoted by F and O, with + and − indicating whether these fluxes are promoting or damping the pressure oscillations. The main impact of the unbalanced momenta is to shift both the stagnation plane

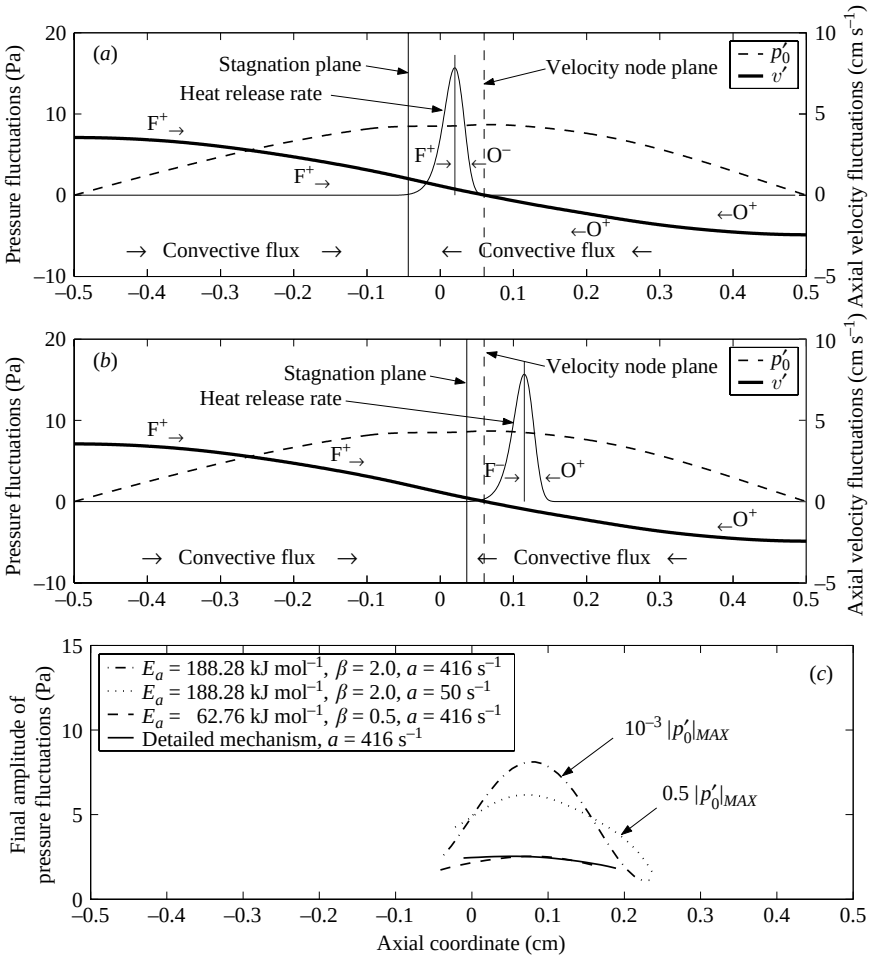


FIGURE 9. Illustration of a counterflow non-premixed flame positioned (*a*) to the left of the velocity node and (*b*) to the right of the velocity node, and (*c*) acoustic response as a function of the location of the flame front ($\alpha = 1$).

and the flame in the same direction, while the location of the velocity node remains nearly the same. Figure 9(*a*) shows the flame front completely to the left of the velocity node, with negative contribution of O, but a positive contribution of F, while figure 9(*b*) shows the flame completely to the right of the velocity node, with negative contribution of F and positive contribution of O. When the flame is in an intermediate position, with the flame structure located across the velocity node, the cancelling effect of the positive and negative fluctuations in the fluxes of reactants is minimized. A velocity node within the reactive–diffuse region of the flame leads to an in-phase modulation of the transport of methane and air, and under certain conditions to a sustained modulation in the heat release rate, e.g. for a thin flame corresponding to a large activation energy. Since the thickness of the reaction layer is somewhat broader for a lower activation energy or the detailed reaction model, cancelling effects are always present and provide a stabilizing effect. For selected values of activation energy for one-step models, by shifting the entire flame structure across the counterflow field, figure 9(*c*) shows that the maximum acoustic pressure

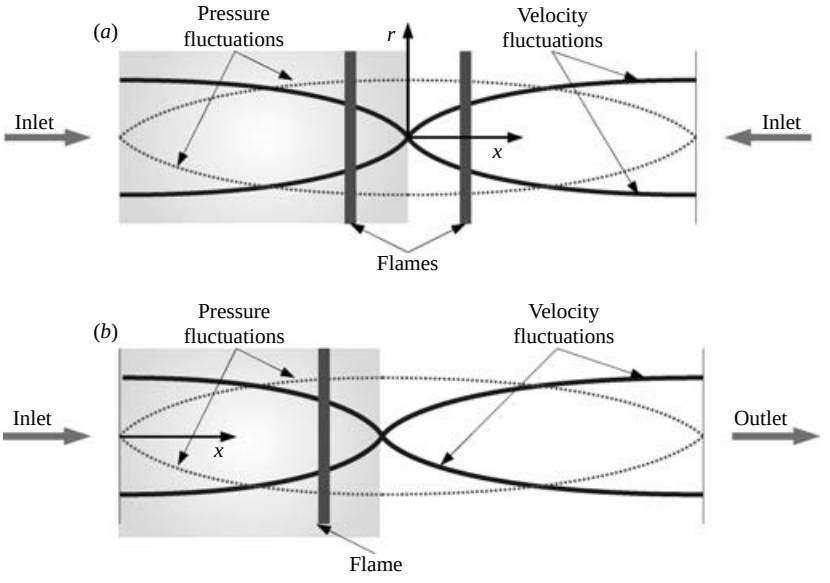


FIGURE 10. Illustration of the similarity between counterflow configuration and tube combustor with respect to oscillations in the mass flux of reactants into the flame. (*a*) Counterflow twin premixed flames. (*b*) Premixed flame in open–open tube.

growth occurs when the flame is near extinction and is located slightly to the oxidizer side with respect to the velocity node. On the other hand, the detailed model predicts three orders of magnitude lower growth (less than 3 Pa after 10 ms), with almost no dependence on the flame location, as seen in figure 9(*c*). In order to overcome the cancelling effect of the fluctuating mass fluxes into the flame front, inherent to the non-premixed structure, the occurrence of flame–acoustics instabilities in a counterflow premixed flame is analysed next.

## 6. Counterflow premixed flames

In the counterflow twin premixed flame configuration illustrated in figure 1(*b*), the locations of the acoustic velocity node and of the stagnation plane coincide at the mid-point of the domain because of the symmetry of the flow field. The position of the premixed flame is a function of the inflow velocity and of the intrinsic laminar burning speed, $S_L^0$, of the premixed fuel–air mixture. Compared to the non-premixed flames considered in § 5, the twin premixed flame configuration offers two main advantages, namely (i) the reaction or heat release layers can be positioned far from the velocity node (see figure 10*a*), and (ii) the fluctuating mass fluxes of reactants, both fuel and oxidizer, into the flame front always promote growth of the instability because the resulting heat release variations are in-phase with pressure oscillation. The latter effect can be explained by direct comparison of the left half of the counterflow twin premixed flame configuration with the upstream half of an open–open Rijke tube (Rijke 1859), as illustrated in figure 10(*b*). Since the acoustic velocity oscillations precede the pressure in the first half of the Rijke tube, placement of a flame in this half always leads to growth of instability (Raun *et al.* 1993), provided the characteristic time scales of the flame and acoustics are matched (see § 7). Similarly to the counterflow non-premixed flames described in the previous section, the influence of chemical reaction models on the acoustic response of the premixed flame is investigated

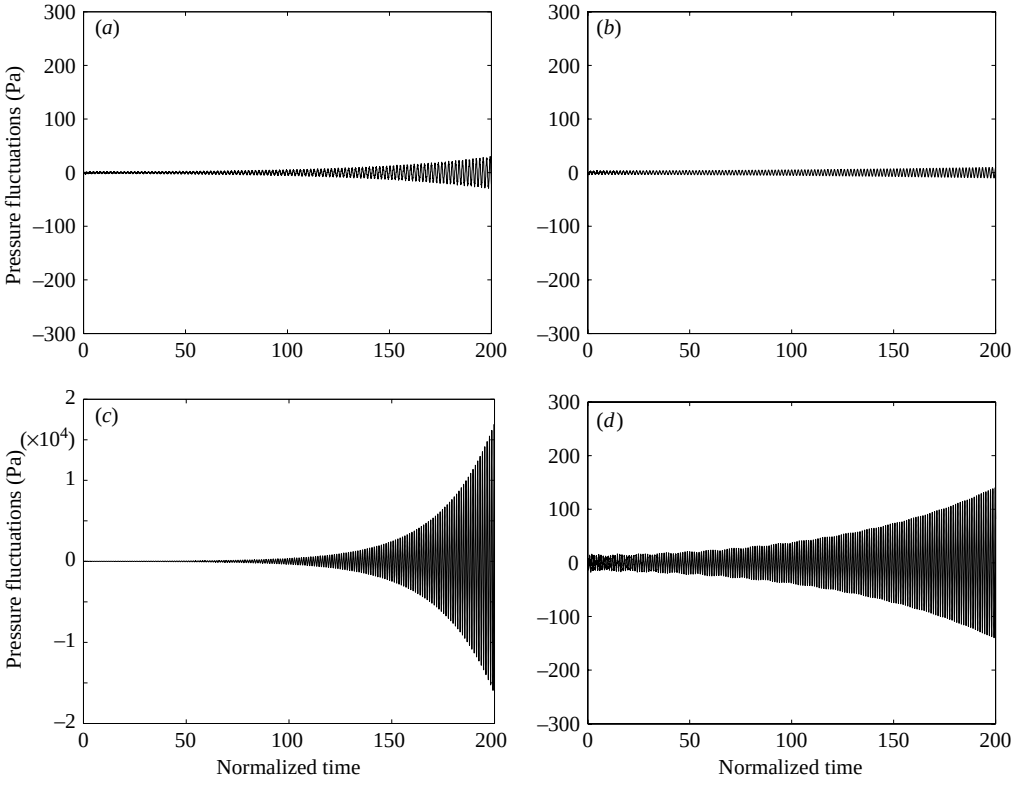


FIGURE 11. Effect of flow strain rate on the acoustic response of counterflow premixed flames using a one-step model with $E_a = 125.5\,\mathrm{kJ\,mol^{-1}}$ and $\alpha = \beta = 1$ and the detailed kinetic model. (*a*) One-step at $a = 220\,\mathrm{s^{-1}}$. (*b*) Detailed at $a = 220\,\mathrm{s^{-1}}$. (*c*) One-step at $a = 1180\,\mathrm{s^{-1}}$. (*d*) Detailed at $a = 1180\,\mathrm{s^{-1}}$.

here. For the one-step model, an independent set of parameters, i.e. $E_a, A, \alpha$ and $\beta$, is obtained to predict the laminar premixed burning speed as well as the flame extinction condition, as described in the Appendix. The predicted acoustic pressure growth obtained with the detailed chemical model is compared to the selected one-step models, for a range of flow strain rates as well as flame locations with respect to the velocity node. Figure 11(*a–d*) shows the evolution in time of the acoustic pressure fluctuations at the mid-point of the domain for strain rates of 220 and $1180\,\mathrm{s^{-1}}$, employing $(a, c)$ a one-step model with $E_a = 125.5\,\mathrm{kJ\,mol^{-1}}$ and $\alpha = \beta = 1.0$, and $(b, d)$ the detailed model. Unlike non-premixed counterflow flames, the acoustic response of premixed counterflow flames always shows a positive growth, regardless of the strain rate or reaction mechanism employed. The predicted growth rate of $p_0'(x, t)$ is enhanced with increasing strain rate, especially for the one-step model considered. To demonstrate the influence of activation energy and the overall reaction order on the growth rate of $p_0'(x, t)$ in counterflow premixed flames, the evolutions in time of the predicted amplitudes of $p_0'(x, t)$ are compared in figure 12$(a, b)$. The growth rate is enhanced as the activation energy or the reaction order are increased. The interesting new result, as shown in figure 11$(b, d)$, is the amplification of pressure fluctuations observed in premixed flames with the detailed model. Although the predicted growth is smaller when compared to the corresponding one-step results, this finding points out that, in premixed counterflow flames, significant coupling between acoustic waves

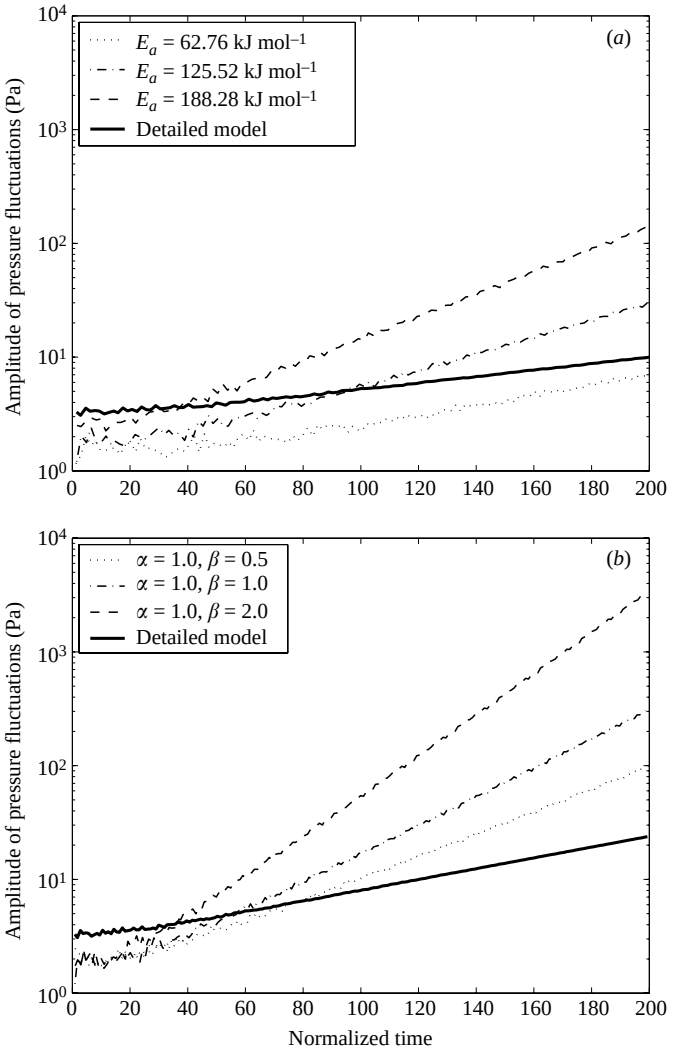


FIGURE 12. Comparison of the acoustic pressure growth rate of a counterflow twin-premixed flame at $a = 220\,\mathrm{s}^{-1}$ between the detailed and one-step kinetic models with (*a*) varying $E_a$ and $\alpha = \beta = 1$, and (*b*) varying $\beta$ and $E_a = 125.5\,\mathrm{kJ\,mol}^{-1}$ and $\alpha = 1$.

and flame dynamics can be established and drive the instabilities. Analysis of the power spectrum indicates that at 10 ms, the predicted sound level for the present premixed flame with detailed kinetic model is about 117 dB, significantly higher than the non-premixed flame prediction of 98 dB discussed in § 5. Introduction of partially reflecting boundary conditions can lower the linear growth rate of $p_0'(x,t)$; however, the self-sustained unsteady pressure oscillations predicted with the detailed model imply that well-designed experiments in counterflow premixed flames have the potential to exhibit such flame–acoustics interactions, whereas computations with non-premixed flames did not indicate this potential, even under the most favourable conditions. As the amplitude of $p_0'(x,t)$ increases, numerical losses or losses at the boundaries in experiments are expected to yield limit-cycle behaviour. Furthermore, the departure from the planar flame approximation may lead to nonlinear growth

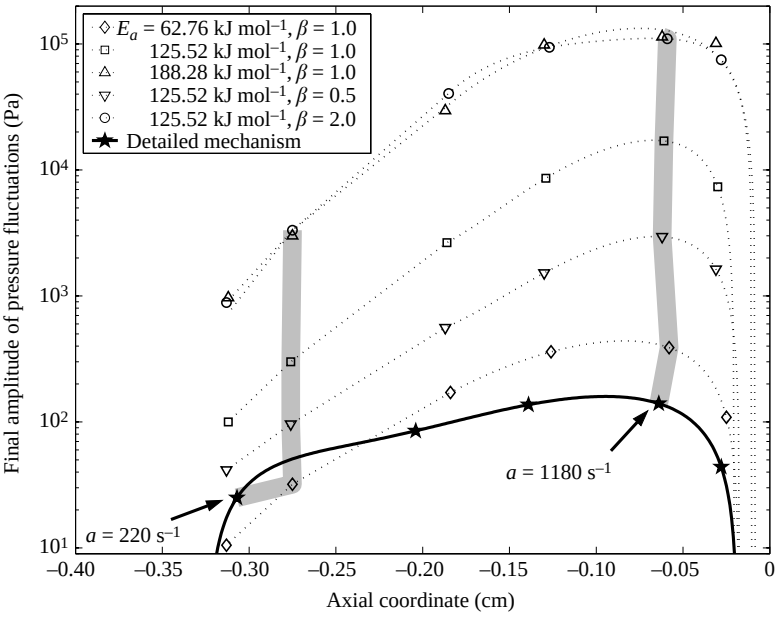


FIGURE 13. Comparison of the pressure amplitude at 10 ms as a function of the flame location (which depends on the flow strain rate), for methane–air counterflow twin premixed flames using different kinetic models ($\alpha = 1$).

of the pressure instability. Experiments by Searby (1992) have clearly shown such transitions from planar self-excited flames to corrugated or cellular flames with much larger amplitudes of $p_0'(x, t)$. The flame stability limits in the presence of pressure variations have been the subject of several theoretical investigations, in particular the spatial pressure gradients effects by Matalon & Matkowsky (1982) and transient bulk pressure effects by Keller & Peters (1994). More recently, in their theoretical work Wu *et al.* (2003) have performed a unified analysis of both spatial and temporal pressure variations on multi-dimensional flames, with the recovery of planar flame–acoustics interaction results of Clavin *et al.* (1990) and others. The most interesting aspect of Wu *et al.*'s (2003) work is the extension to the nonlinear growth regime associated with non-planar flames, similar to the recent computational work reported by Teerling *et al.* (2005). Unfortunately, all the above work, including the computational work by Teerling *et al.* (2005), has assumed one-step irreversible reaction models with large activation energy and exothermic heat release and, as shown here, the predicted flame-acoustic coupling can differ greatly from the detailed reaction model.

### 6.1. *Effect of premixed flame location*

In the counterflow premixed flames considered here, for a selected fuel–air composition, the flame location with respect to the stagnation plane or point (which is same as the acoustic velocity node) directly depends on the imposed flow strain rate, as shown in figure 13. Because of the relatively high extinction strain rate of premixed flames (about 2100 s$^{-1}$, see figure 17 below), these flames allow much greater flexibility in investigating the effect of flame location with respect to the stagnation plane and the dynamic response of the flame to velocity variations. As shown in figure 13, the maximum flame–acoustics interaction is clearly seen to occur away from the stagnation plane and at a considerably lower strain rate (about 1180 s$^{-1}$)

than the extinction strain rate. As the counterflow twin premixed flames approach the stagnation plane at extremely high strain rates, because of the velocity node located at the mid-point, the predicted growth rate is diminished. This observation is consistent with premixed flames positioned in Rijke tubes, where the peak growth rate is observed at one quarter of the length from the inlet for an open-open tube. While the predicted growth rate varies by several orders of magnitude between reaction models, the effect of flame location is consistent for all the models.

## 7. Analysis of time scales and heat release

### 7.1. *Characteristic time scales*

Flame–acoustics interactions arise when the characteristic acoustic time scales of the flow configuration are matched with the time scales of the flame and when heat release rate fluctuations are in-phase with acoustic pressure fluctuations. Assuming that pressure nodes are located at the exits of the nozzles, the dominant acoustic time scale in the present counterflow geometry can be estimated by $\tau_{acou} = 2l/\bar{c}$, where $\bar{c}$ is the mean speed of sound. While the acoustic velocity varies across the thermal mixing layer, the numerical calculations show that the acoustic time scale is primarily a function of the separation distance between the opposed nozzles, $l$. In other words, for a fixed nozzle separation distance of $l = 1$ cm, $\tau_{acou} \sim 3 - 5 \times 10^{-5}$ s, indicating only a minor variation due to thermal mixing layer changes with flow strain rate. Two other characteristic time scales can be identified for the flame, namely $\tau_{transp}$, associated with the balance of convective and diffusive processes in the transport zones, and $\tau_{chem}$, associated with the thin reactive–diffusive zone. These flame time scales vary considerably across the flame and local values are estimated based on the flame structure results, e.g. from (2.4) the diffusion time-scale of methane, $\tau_{diff,CH_4} = \rho Y_{CH_4}/|\partial(\rho V_{CH_4} Y_{CH_4})/\partial x|$ (see figure 14).

In the context of one-step reaction models, the acoustic response of a laminar flame to external pressure perturbations was analysed by McIntosh (1991) and Clavin *et al.* (1990) in terms of the scalings of $\tau_{transp}$ and $\tau_{chem}$ with respect to $\tau_{acou}$. The scalings of interest to the present investigation are (i) $\tau_{transp}/\tau_{acou} \sim 1$, when acoustic waves at intermediate frequencies result in an unsteady response of the transport zone, and (ii) $\tau_{chem}/\tau_{acou} \sim 1$ (or $\tau_{transp}/\tau_{acou} \sim \theta^2$, with $\theta$ the non-dimensional activation energy), when acoustic waves at high frequencies result in an unsteady response of the reaction zone. Figure 14 shows the evaluated flame and acoustic time scales of a non-premixed flame and a premixed flame using the one-step model with $\alpha = \beta = 1.0$ and $E_a = 125.5$ kJ mol$^{-1}$. These time-scale profiles are representative of the other one-step kinetic models. While in non-premixed flames, two distinct convective–diffusive transport zones, for $CH_4$ and $O_2$ respectively, exist on each side of the reactive–diffusive zone, in premixed flames a single reactant transport zone precedes the reactive–diffusive zone. The two transport time scales of the non-premixed flame can be determined from $\tau_{transp,CH_4} \approx \tau_{diff,CH_4}$ of the convective–diffusive layer on the fuel side and from $\tau_{transp,O_2} \approx \tau_{diff,O_2}$ of the convective–diffusive layer on the oxidizer side. In contrast, premixed flames have a single convective–diffusive layer with $\tau_{transp} \approx \tau_{diff,CH_4} \approx \tau_{diff,O_2}$. A summary of the time scalings for each layer, evaluated at the minima of each profile, is provided in table 1 for non-premixed flames and in table 2 for premixed flames, for two strain rates and the reaction models employed.

For non-premixed flames, $\tau_{transp,CH_4}$ and $\tau_{transp,O_2}$ decreases with increasing strain rate owing to the reduced mixing layer thickness, as seen in table 1. At each selected strain rate (50 and 416 s$^{-1}$), these transport time scales are clearly invariant with the

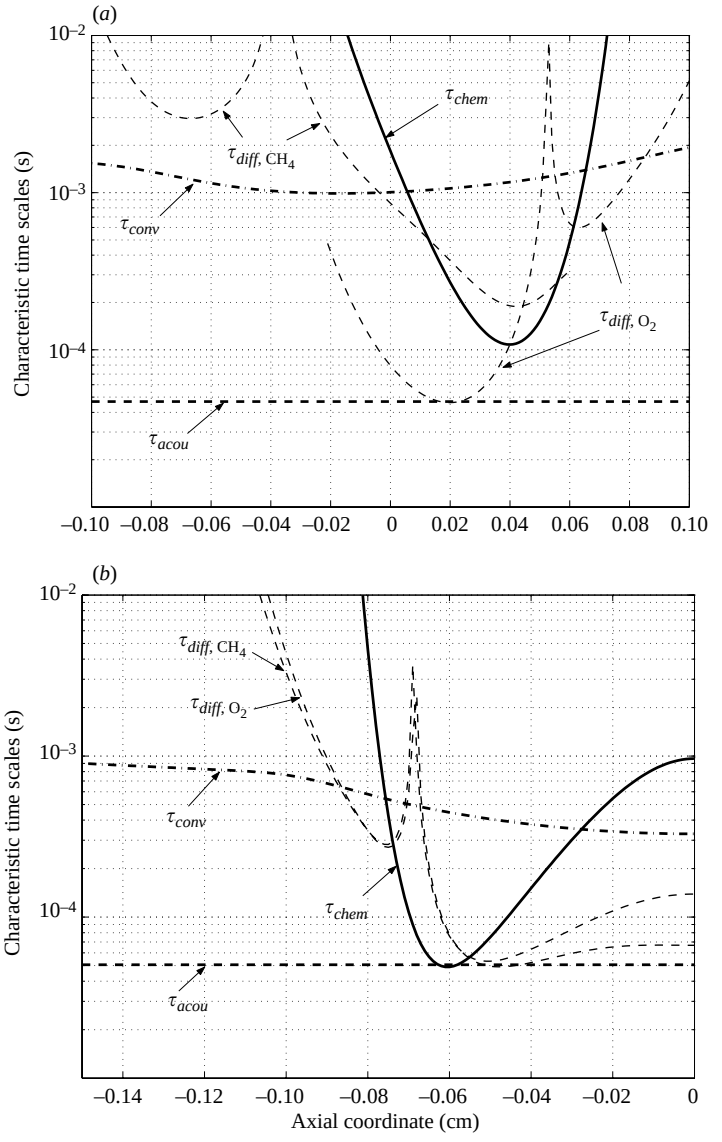


FIGURE 14. Characteristic time scales across the flame structure of a counterflow (*a*) non-premixed at $a = 416\,\mathrm{s}^{-1}$ and (*b*) a premixed flame at $a = 1180\,\mathrm{s}^{-1}$, employing a one-step kinetic model with $\alpha = \beta = 1.0$ and $E_a = 125.5\,\mathrm{kJ\,mol}^{-1}$.

chemical parameters adopted, except for the transport time-scale associated with $O_2$ at a near-extinction strain rate of $416\,\mathrm{s}^{-1}$. The latter variation is due to the change in flame structure, namely the increased oxygen leakage leading to the variation of the oxidizer gradient, $\partial Y_{O_2}/\partial x$ for the one-step models. In particular, this gradient is affected by the shift of the fuel-side edge of the oxidizer consumption layer further into the fuel stream with decreasing activation energy, resulting in a shallower gradient. With increasing strain rate and activation energy of the one-step model, the limit $\tau_{chem}/\tau_{acou} \rightarrow 1$, corresponding to the high-frequency regime identified by McIntosh (1999), is the primary cause for a significant growth of the acoustic pressure fluctuations, $p_0'(x, t)$ (see figure 7*a*).

| $E_a$ | $\alpha$ | $\beta$ | $\tau_{transp,\,CH_4}/\tau_{acou}$ Strain rate | | $\tau_{transp,O_2}/\tau_{acou}$ Strain rate | | $\tau_{chem}/\tau_{acou}$ Strain rate | |
|---|---|---|---|---|---|---|---|---|
| | | | $50\,s^{-1}$ | $416\,s^{-1}$ | $50\,s^{-1}$ | $416\,s^{-1}$ | $50\,s^{-1}$ | $416\,s^{-1}$ |
| 62.8(15) | 1.0 | 1.0 | 750 | 67 | 50 | 28.9 | 12.5 | 6.7 |
| 125.5(30) | 1.0 | 1.0 | 750 | 67 | 50 | 13.3 | 6.3 | 2.7 |
| 188.3(45) | 1.0 | 1.0 | 750 | 67 | 50 | 8.9 | 5.0 | 1.6 |
| Detailed | | | 750 | 67 | 50 | 12.2 | – | – |

TABLE 1. Summary of characteristic time-scale ratios for a counterflow non-premixed flame at $a = 50\,s^{-1}$ and $a = 416\,s^{-1}$ employing the one-step and the detailed kinetic models. Units of $E_a$ are kJ mol$^{-1}$ (in parenthesis kcal mol$^{-1}$).

| $E_a$ | $\alpha$ | $\beta$ | $\tau_{transp,\,CH_4}/\tau_{acou}$ Strain rate | | $\tau_{transp,O_2}/\tau_{acou}$ Strain rate | | $\tau_{chem}/\tau_{acou}$ Strain rate | |
|---|---|---|---|---|---|---|---|---|
| | | | $220\,s^{-1}$ | $1180\,s^{-1}$ | $220\,s^{-1}$ | $1180\,s^{-1}$ | $220\,s^{-1}$ | $1180\,s^{-1}$ |
| 62.8(15) | 1.0 | 1.0 | 20 | 13 | 20 | 13 | 2.9 | 1.8 |
| 125.5(30) | 1.0 | 1.0 | 8.6 | 6 | 8.6 | 6 | 1.4 | 1.0 |
| 188.3(45) | 1.0 | 1.0 | 5.7 | 4 | 5.7 | 4 | 1.0 | 0.7 |
| Detailed | | | 5.7 | 3 | 6.6 | 5 | – | – |

TABLE 2. Summary of characteristic time-scale ratios for counterflow twin premixed flames at $a = 220\,s^{-1}$ and $a = 1180\,s^{-1}$ employing the one-step and the detailed kinetic models. Units of $E_a$ are kJ mol$^{-1}$ (in parenthesis kcal mol$^{-1}$).

Comparison of $\tau_{transp,O_2}$ between one-step models and the detailed model indicate that the oxidizer transport zone predicted by the detailed model is very similar to that of the 125.5 kJ mol$^{-1}$ one-step model, even though the flame response to acoustic waves is much weaker. Furthermore, owing to the wide range of chemical time scales in the detailed model, an in-depth analysis of the heat release rate contributions and of the activation energy associated with each reaction is required (see § 7.2).

As shown in table 2, the transport zone of steady twin counterflow premixed flames, in contrast to the weakly strained non-premixed flames (near equilibrium), must respond to any chemical kinetic parameter variations. While the flame structure and the time scales change with flow strain rate, similarly to the non-premixed flame, the dynamic balance is critical in maintaining steady counterflow premixed flames. With increasing activation energy, the limit $\tau_{chem}/\tau_{acou} \to 1$ is easily satisfied, providing a mechanism for establishing high-frequency flame–acoustics interactions. Once again, the detailed mechanism encompasses a wide range of time scales; however, as seen from figure 12, the degree of interaction is weaker compared to one-step models with a large activation energy.

### 7.2. *Exothermicity/endothermicity of reactions*

For both counterflow non-premixed and premixed flames, the time-scale analysis indicates no significant differences between the one-step and the detailed models, apart from the large activation energy promoting the coupling, consistent with previous theoretical studies of McIntosh (1991). The effect of large activation energy on the sensitivity of the heat release rate to acoustic disturbances can be explained by the exponential dependence of the reaction rate on temperature fluctuations, i.e.

$$\omega \propto \exp(-E_a/R^o T) \simeq \exp(-\theta(1 - \Delta T/T)), \tag{7.1}$$

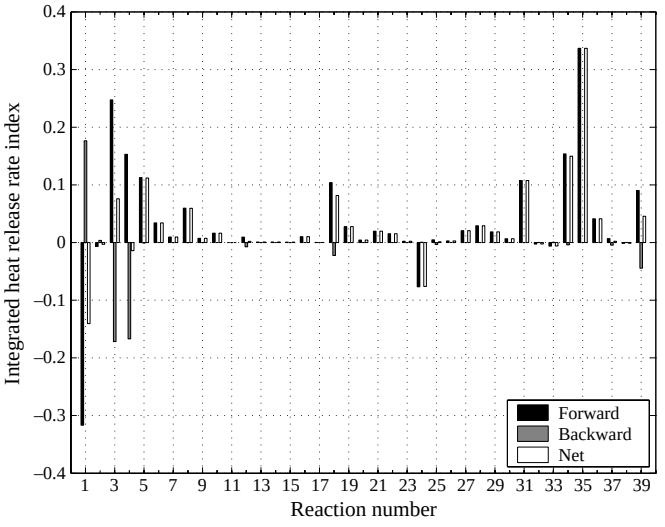


FIGURE 15. Integrated heat release index for forward and backward reaction steps, and for the net contribution of each elementary reaction.

where $\Delta T$ is the temperature perturbation and $\theta = E_a/R^\circ T$. Therefore, any exothermic reaction with large $\theta$ can promote the growth of pressure fluctuations. Since by definition one-step irreversible reactions are always exothermic, it is not surprising that such one-step global models predict significant growth of $p_0'(x,t)$, assuming that the time scales and flame locations are favourable. In contrast, in the detailed model, the most rate-controlling large-activation-energy reactions are endothermic. Under such conditions, the endothermicity of the reaction out-of-phase with pressure fluctuations dampens the flame–acoustics interactions. This difference between the one-step model and the detailed model, i.e. the exothermicity or endothermicity of reactions, can explain the predicted results.

For the present methane–air detailed reaction model, an analysis of the heat release rate, $\dot{q}_j$ of each reaction $j$, is carried out and only the results for the non-premixed flame at the near-extinction strain rate of $416\,\mathrm{s}^{-1}$ are shown in figure 15. It is interesting to note that reaction 35 (forward) ($CH_3 + O \rightarrow CH_2O + H$), which contributes most to the exothermic heat release, has a zero activation energy. On the other hand, reaction 32 (forward) ($CH_2O + M \rightarrow HCO + H + M$), featuring the largest value of activation energy ($320\,000\,\mathrm{J\,mol}^{-1}$), is endothermic and hence dampens the flame–acoustics coupling. Reaction 1 ($H + O_2 \rightleftarrows OH + O$) has a significant endothermicity associated with the forward rate ($E_{a,f} = 70\,310\,\mathrm{J\,mol}^{-1}$) while the reverse rate, associated with exothermicity, has activation energy of only $3\,520\,\mathrm{J\,mol}^{-1}$, with the net effect damping the flame–acoustics coupling. The above hypothesis on coupled effects of large activation energy and exothermicity cannot be easily verified by using a detailed reaction model having complex reaction pathways. Instead, constructing an appropriate two-step reaction model with the flexibility to systematically uncouple the effects of exothermicity and large activation energy may provide a suitable mechanism to verify the above results and should be pursued in the future.

## 8. Conclusions

Previous theoretical investigations on flame–acoustics interactions have provided fundamental information about the characteristic time scales promoting coupling, the

influence of activation energy and the effects of reaction orders. These analyses were performed either by treating the flame as a gasdynamic discontinuity or by using simple one-step irreversible reaction models. The unsteady pressure was assumed uniform in space and therefore independent of the flow configuration, requiring the introduction of external pressure or velocity perturbations.

By employing the simple counterflow geometry, the present work has addressed two major aspects of flame–acoustics interactions not considered in previous theoretical studies, namely (i) the geometry-dependent self-sustained flame–acoustics interactions, and (ii) the inclusion of detailed chemical reaction models with realistic heat release mechanisms. In the counterflow configuration, the occurrence of the self-excited amplification of pressure fluctuations was shown to depend on the flame location with respect to the acoustic pressure and velocity nodes, as well as on the phasing of the reactant flux with respect to the pressure oscillations. These flame location effects were effectively demonstrated in counterflow non-premixed and premixed flames, due to the distinct phase differences of the reactant flux terms.

Besides flame location effects, the results presented here highlight the importance of using a realistic reaction model with accurate representation of the heat release terms. The numerical predictions with the realistic model (i.e. the detailed reaction model) were compared with a set of one-step global reaction models with varying activation energy and reaction orders. The collision frequency term of the one-step model was selected to predict flame propagation and extinction in fair agreement with the detailed model. These one-step irreversible global models with exothermic heat release clearly highlighted the effect of activation energy and overall reaction orders on the flame–acoustics coupling mechanism. In contrast, the detailed reaction model with 39 reversible reactions and comprising a wide range of exothermicity/endothermicity and activation energies showed a considerably weaker amplification of the pressure fluctuations for counterflow premixed flames (117 dB after 10 ms and at a strain rate of $220\,s^{-1}$) and almost no amplification for non-premixed flames (98 dB after 10 ms and at a strain rate of $416\,s^{-1}$).

This work was partially supported by the Virginia Space Grant Consortium through the Aerospace Graduate Research Fellowship Program and by the National Science Foundation under grant No. ITR-046971.

## Appendix. One-step global reaction rate parameters

For methane–air flames, a set of reaction rate parameters for the one-step model, namely the reaction orders $\alpha$ and $\beta$ with respect to the fuel and oxidizer, and the activation energy, $E_a$, are derived and compared to the detailed kinetic model of Peters & Rogg (1993). The purpose of this is to explore the sensitivity of the reaction rate parameters to the flame–acoustics interactions. In deriving the one-step kinetic rate constants, the pre-exponential term or the effective collision frequency, $A$, is adjusted such that the same flame extinction condition or the burning speed as the detailed model is obtained. Consequently, the fluid-dynamical aspects of the flow under investigation remain the same, e.g. the thickness of the mixing layer; however, the flame temperature can vary.

For a steady, laminar methane–air non-premixed flame, figure 16 shows a comparison of the peak flame temperature as a function of the strain rate, predicted using the detailed reaction model as well as the one-step models derived, showing the effects of varying ($a$) activation energy, $E_a$, while keeping $\alpha = \beta = 1$, and

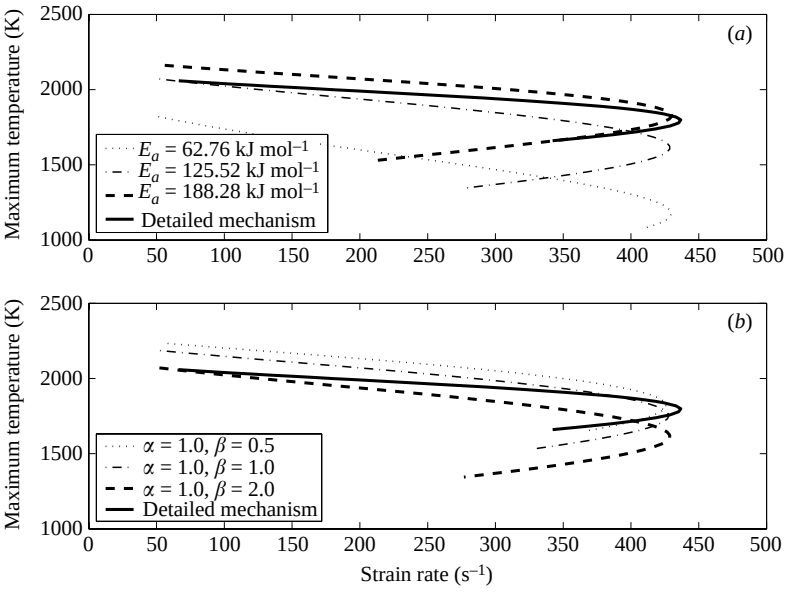


FIGURE 16. Comparison of predicted peak temperature as a function of strain rate for counterflow methane–air non-premixed flames between the detailed model and three one-step models with (*a*) varying $E_a$ and $\alpha = \beta = 1$, and (*b*) varying $\beta$ and $E_a = 125.5\,\mathrm{kJ\,mol^{-1}}$ and $\alpha = 1$.

| $E_a$ | $\alpha$ | $\beta$ | $A$ | |
|---|---|---|---|---|
| | | | Non-premixed | Premixed |
| 62.8(15) | 1.0 | 1.0 | $2.90 \times 10^{11}$ | $1.42 \times 10^{12}$ |
| 125.5(30) | 1.0 | 0.5 | $2.80 \times 10^{10}$ | $1.61 \times 10^{11}$ |
| 125.5(30) | 1.0 | 1.0 | $5.50 \times 10^{13}$ | $2.48 \times 10^{14}$ |
| 125.5(30) | 1.0 | 2.0 | $1.35 \times 10^{20}$ | $4.48 \times 10^{20}$ |
| 188.3(45) | 1.0 | 1.0 | $4.50 \times 10^{15}$ | $1.97 \times 10^{16}$ |

TABLE 3. Summary of chemical kinetic parameters used in one-step models for counterflow non-premixed and premixed flames. Units of $E_a$ are kJ mol$^{-1}$ (kcal mol$^{-1}$).

(*b*) reaction order, $\beta$, while keeping $E_a = 125.5\,\mathrm{kJ\,mol^{-1}}$ and $\alpha = 1$. With regard to reaction orders, here only the variation of $\beta$ is considered because the sensitivity analysis has indicated that the perturbation of $\beta$ has a dominant effect compared to that of $\alpha$. These sensitivity results are not shown here for brevity. A summary of one-step model kinetic parameters derived for methane–air non-premixed flames is shown in table 3.

For methane–air premixed flames, a similar derivation of reaction rate parameters is conducted based on the extinction condition of twin counterflow premixed flames (see figure 17) as well as on the laminar flame propagation velocity, $S_L^0$, of steady, one-dimensional, freely propagating flames (see figure 18). A unique set of pre-exponential terms for premixed flames that satisfy both the laminar burning speed and the extinction strain rate is nearly impossible because of the *ad hoc* nature of these one-step models and a compromise must be made. For the present unsteady flame–acoustics investigation, in order to perform an analysis of kinetic parameters,

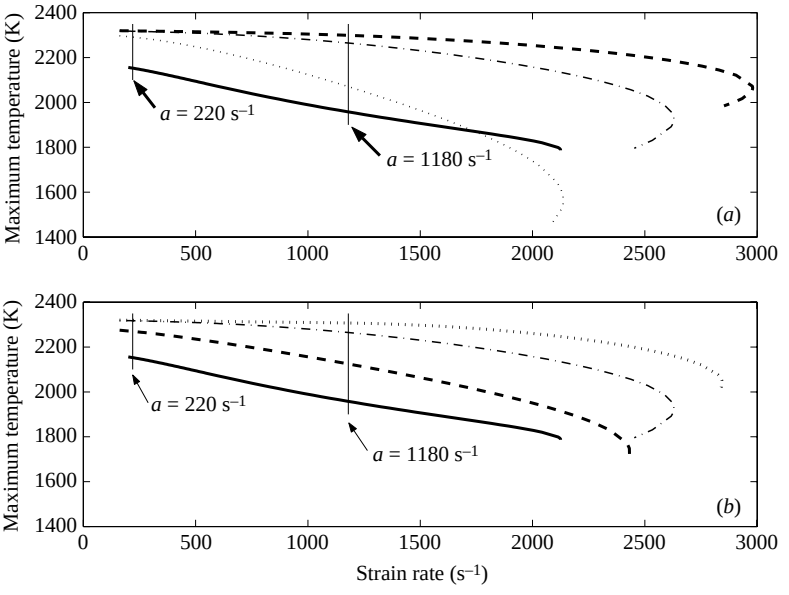


FIGURE 17. Comparison of predicted peak temperature as a function of strain rate for counterflow methane–air twin premixed flames at stoichiometric conditions between the detailed model and three one-step models with (*a*) varying $E_a$ and $\alpha = \beta = 1$, and (*b*) varying $\beta$ and $E_a = 125.5\,\mathrm{kJ\,mol^{-1}}$ and $\alpha = 1$. Symbols as figure 16.

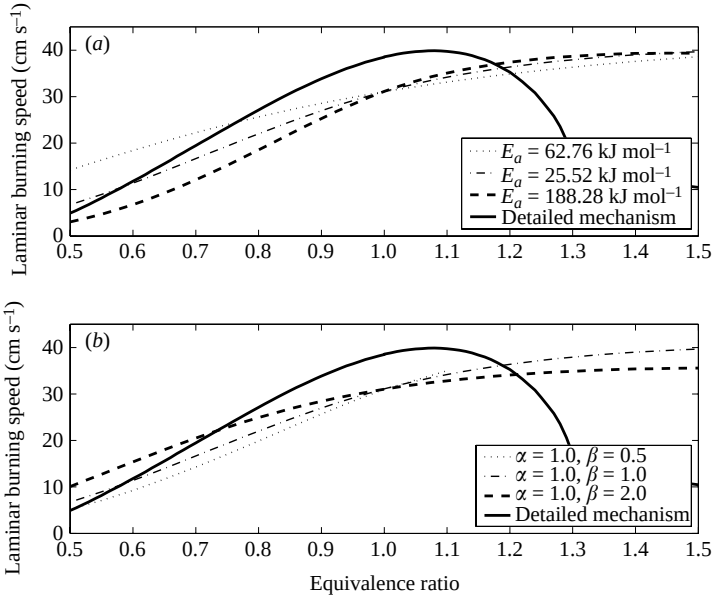


FIGURE 18. Comparison of predicted laminar burning speed as a function of equivalence ratio for a methane–air mixture between the detailed model and three one-step models with (*a*) varying $E_a$ and $\alpha = \beta = 1$, and (*b*) varying $\beta$ with $E_a = 125.5\,\mathrm{kJ\,mol^{-1}}$ and $\alpha = 1$.

it is important to have the flame at the same location in the counterflow field for a selected flow strain rate. The premixed flame property that satisfies this criterion is the burning velocity, hence as a compromise the pre-exponential terms are selected

such that, at stoichiometric conditions, a burning velocity of $31\,\mathrm{cm\,s^{-1}}$ is realized, as shown in figure 18. Consequently, for counterflow premixed flames, the predicted extinction strain rate ranges from 2000 to $3000\,\mathrm{s^{-1}}$ as shown in figure 17. A summary of one-step model kinetic parameters derived for methane–air premixed flames is also shown in table 3.

It should be pointed out that one-step reaction models cannot predict the decrease in $S_L^0$ for rich premixed flames (equivalence ratio greater than unity), unless a reaction order less than unity is selected for the fuel, as shown by Westbrook & Dryer (1981).

## REFERENCES


Brown, T., Pitz, R. & Sung, C. 1998 Oscillatory stretch effects on the structure and extinction of counterflow diffusion flames. *Proc. Combust. Inst.* **27**, 703–710.

Candel, S., Huynh, C. & Poinsot, T. 1996 Some modeling methods of combustion instabilities. In *Unsteady Combustion* (ed. F. Culick, M. Heitor & J. Whitelaw), pp. 83–112. Kluwer.

Chelliah, H., Law, C., Ueda, T., Smooke, M. & Williams, F. 1990 An experimental and theoretical investigation of flow-field, dilution and pressure effects on the extinction condition of methane/oxygen/nitrogen diffusion flames. *Proc. Combust. Inst.* **23**, 503–511.

Chelliah, H., Seshadri, K. & Law, C. 1993 Reduced kinetic mechanisms for counterflow methane diffusion flames. In *Reduced Kinetic Mechanisms for Applications in Combustion Systems* (ed. N. Peters & B. Rogg). Lecture Notes in Physics, vol. 15, pp. 224–240. Springer.

Chu, B. 1953 On the generation of pressure waves at a plane flame front. *Fourth Symposium (Intl) on Combustion*, vol. 4, 603–612. The Combustion Institute.

Clavin, P., Pelcé, P. & He, L. 1990 One-dimensional vibratory instability of planar flames propagating in tubes. *J. Fluid. Mech.* **216**, 299–322.

Darabiha, N. 1992 Transient behaviour of laminar counterflow hydrogen-air diffusion flames with complex chemistry. *Combust. Sci. Tech.* **86**, 163–181.

Durox, D., Schuller, T. & Candel, S. 2002 Self-induced instability of a premixed jet flame impinging on a flame. *Proc. Combust. Inst.* **29**, 69–75.

Egolfopoulos, F. & Campbell, C. 1996 On the structure and dynamics of unsteady, counterflowing, strained diffusion flames: diffusion-limited frequency response. *J. Fluid Mech.* **318**, 1–29.

Fletcher, C. 1988 *Computational Techniques for Fluid Dynamics*, 2nd edn. Springer.

Garris, C., Toong, T.-Y. & Patureau, J.-P. 1975 Chemi-acoustic instability structure in irreversibly reacting systems. *Acta Astronautica* **2**, 981–997.

van Harten, A., Kapila, A. & Matkowsky, B. 1984 Acoustic coupling of flames. *SIAM J. Appl. Maths* **44** (5), 982–995.

Im, H., Law, C., Kim, J. & Williams, F. 1995 Response of counterflow diffusion flames to oscillating strain rates. *Combust. Flame* **100**, 21–30.

Keller, D. & Peters, N. 1994 Transient pressure effects in the evolution equation for premixed flame fronts. *Theor. Comput. Fluid Dyn.* **6**, 141–159.

Kim, J. & Williams, F. 1994 Contribution of strained diffusion flames to acoustic pressure response. *Combust. Flame* **98**, 279–299.

Matalon, M. & Matkowsky, B. 1982 Flames as gasdynamic discontinuities. *J. Fluid Mech.* **124**, 239–259.

Mauss, F. & Peters, N. 1993 Reduced kinetic mechanisms for premixed methane-air flames. In *Reduced Kinetic Mechanisms for Applications in Combustion Systems* (ed. N. Peters & B. Rogg). Lecture Notes in Physics, vol. 15, pp. 58–75. Springer.

McIntosh, A. 1991 Pressure disturbances of different length scales interacting with conventional flames. *Combust. Sci. Tech.* **75**, 287–309.

McIntosh, A. 1999 Deflagration fronts and compressibility. *Phil. Trans. R. Soc. Lond.* A **357**, 3523–3538.

McIntosh, A., Brindley, J. & Yang, X.-S. 2002 Pressure disturbances and strained premixed flames. *Combust. Theory Modelling* **6**, 35–51.

Oran, E. & Gardner, J. 1985 Chemical-acoustic interactions in combustion systems. *Prog. Energy. Combust. Sci.* **11**, 253–276.

Pandya, T. & Weinberg, F. 1963 Techniques for analyzing and stabilizing laminar diffusion flame structures, taking heat release and composition into account. *Ninth Symposium (Intl) on Combustion*, vol. 9, 587–596. The Combustion Institute.

Peters, N. & Rogg, B. (Eds.) 1993 *Reduced Kinetic Mechanisms for Applications in Combustion Systems*. Lecture Notes in Physics, vol. 15. Springer.

Poinsot, T. & Lele, S. 1992 Boundary conditions for direct simulations of compressible viscous flows. *J. Comput. Phys.* **101**, 104–129.

Potter Jr., A. & Butler, J. 1959 A novel combustion measurement based on the estinguishment of diffusion flames. *Am. Rocket Soc.* **29**, 54–56.

Raun, R., Beckstead, M., Finlinson, J. & Brooks, K. 1993 A review of rijke tubes, rijke burners and related devices. *Prog. Energy Combust. Sci.* **19**, 313–364.

Rayleigh, Lord 1878 The explanation of certain acoustical phenomena. *Nature* **18**, 319–321.

Rijke, P. 1859 Notice of a new method of causing vibration of the air contained in a tube open at both ends. *Phil. Mag.* **17** (IV), 419–422.

Rogg, B. 1989 Numerical modelling and computation of reactive stagnation-point flows. In *Computers and Experiments in Fluid Flow* (ed. G. Carlomagno & C. Brebbia), vol. 75, pp. 75–85. Springer.

Searby, G. 1992 Acoustic instability in premixed flames. *Combust. Sci. Tech.* **81**, 221–231.

Seshadri, K. & Williams, F. 1978 Laminar flow between parallel plates with injection of a reactant at high Reynolds number. *Intl J. Heat Mass Transfer* **21**, 251–253.

Smooke, M., Crump, J., Seshadri, K. & Giovangigli, V. 1990 Comparison between experimental measurements and numerical calculations of the structure of counterflow, diluted, methane–air, premixed flames. *Proc. Combust. Inst.* **23** (ME-100-90), 463–473.

Sohn, C. H. 2002 Unsteady analysis of acoustic pressure response in $N_2$ diluted $H_2$ and air diffusion flames. *Combust. Flame* **128**, 111–120.

Teerling, O., McIntosh, A., Brindley, J. & Tam, V. 2005 Premixed flame response to oscillatory pressure waves. *Proc. Combust. Inst.* **30**, 1733–1740.

Toong, T.-Y., Arbeau, P., Garris, C. & Patureau, J.-P. 1975 Acoustic–kinetic interactions in an irreversibly reacting medium. *Fifteenth Symposium (Intl) on Combustion*, vol. 15, 87–100. The Combustion Institute.

Tsuji, H. 1982 Counterflow diffusion flames. *Prog. Energy Combust. Sci.* **8**, 93–119.

Westbrook, C. & Dryer, F. 1981 Simplified reaction mechanisms for the oxidation of hydrocarbon fuels in flames. *Combust. Sci. Tech.* **27**, 31–43.

Williams, F. 1985 *Combustion Theory*. Addison-Wesley.

Wu, X., Wang, M., Moin, P. & Peters, N. 2003 Combustion instability due to the nonlinear interaction between sound and flame. *J. Fluid Mech.* **497**, 23–53.

Zambon, A. 2005 Modeling of thermo-acoustic instabilities in counterflow flames. PhD thesis, University of Virginia.